JNeurosci
THE JOURNAL OF NEUROSCIENCE

Research Articles: Systems/Circuits

Cell-type and endocannabinoid specific synapse connectivity in the adult nucleus accumbens core

https://doi.org/10.1523/JNEUROSCI.1100-19.2019

Cite as: J. Neurosci 2019; 10.1523/JNEUROSCI.1100-19.2019

Received: 14 May 2019
Revised: 4 December 2019
Accepted: 5 December 2019

Cell-type and endocannabinoid specific synapse connectivity in the adult nucleus accumbens core

ABBREVIATED TITLE: Pathway connectivity in the nucleus accumbens core

Marion A. Deroche [1,2,3*], Olivier Lassalle [1,2,3] Laia Castell[4], Emmanuel Valjent[4] and Olivier J. Manzoni [1,2,3,*]

[1] INMED, INSERM U1249, Marseille, France.
[2] Aix-Marseille University, France.
[3] Cannalab, Cannabinoids Neuroscience Research International Associated Laboratory. INSERM-Indiana University, Bloomington Indiana, USA.
[4] IGF, CNRS, INSERM, University of Montpellier, Montpellier, France.

[*]Corresponding author: olivier.manzoni@inserm.fr

Number of pages: 35.
Number of Figures: 9; Tables: 0.
Number of words for Abstract: 204; Introduction: 672; Discussion: 984.

CONFLICT OF INTEREST: The authors declare no conflict of interest.

ACKNOWLEDGMENTS: The authors are grateful to Dr. Pascale Chavis and members of the Chavis-Manzoni laboratory for helpful discussions, Dr. Andrew Scheyer for correcting the manuscript, Steeve Maldera for experimental help, Dr. Daniela Neuhofer for initiating the project and to the National Institute of Mental Health's Chemical Synthesis and Drug Supply Program (Rockville, MD, USA).

AUTHOR CONTRIBUTIONS: MD, OL, EV and OJM designed research; MD, OL and LC performed research; MD, OL, LC and EV analyzed data; MD and OJM wrote the paper.

FUNDING: This work was supported by the Institut National de la Santé et de la Recherche Médicale (INSERM); Fondation pour la Recherche Médicale (Equipe FRM 2015 to OJM) and the NIH (R01DA043982).

ABSTRACT

The nucleus accumbens (NAc) is a mesocorticolimbic structure that integrates cognitive, emotional and motor functions. Although its role in psychiatric disorders is widely acknowledged, the understanding of its circuitry is not complete. Here we combined optogenetic and whole-cell recordings to draw a functional portrait of excitatory disambiguated synapses onto D1 and D2 medium spiny neurons (MSNs) in the adult male mouse NAc core. Comparing synaptic properties of ventral hippocampus (vHipp), basolateral amygdala (BLA) and prefrontal cortex (PFC) inputs revealed a hierarchy of synaptic inputs that depends on the identity of the postsynaptic target MSN. Thus, the BLA is the dominant excitatory pathway onto D1 MSNs (BLA > PFC = vHipp) while PFC inputs dominate D2 MSNs (PFC > vHipp > BLA). We also tested the hypothesis that endocannabinoids endow excitatory circuits with pathway- and cell-specific plasticity. Thus, while CB1 receptors (CB1R) uniformly depress excitatory pathways irrespective of MSNs identity, TRPV1 receptors (TRPV1R) bidirectionally control inputs onto the NAc core in a pathway-specific manner. Finally, we show that the interplay of TRPV1R/CB1R shapes plasticity at BLA-NAc synapses. Together these data shed new light on synapse and circuit specificity in the adult NAc core and illustrate how endocannabinoids contribute to pathway-specific synaptic plasticity.

SIGNIFICANCE STATEMENT

We examined the impact of connections from the ventral hippocampus (vHipp,) basolateral amygdala (BLA) and prefrontal cortex (PFC) onto identified medium spiny neurons (MSN) in the adult accumbens core. We found BLA inputs were strongest at D1 MSNs while PFC inputs dominate D2 MSNs. Pathway- and cell-specific circuit control was also facilitated by endocannabinoids that endow bidirectional synaptic plasticity at identified BLA-NAc synapses. These data provide mechanistic insights on synapse and circuit specificity in the adult NAc core.

INTRODUCTION

The nucleus accumbens (NAc) is a mesocorticolimbic structure (Humphries and Prescott, 2010) that integrates cognitive, emotional and motor functions (Floresco, 2015). Although the NAc's role in neurological and psychiatric disorders including anxiety, depression, addiction and intellectual disability (Goto and Grace, 2008; Kasanetz et al., 2010; Sesack and Grace, 2010; Lafourcade et al., 2011; Jung et al., 2012; Neuhofer et al., 2015, 2018; Bosch-Bouju et al., 2016; Manduca et al., 2017) is widely acknowledged (Salgado and Kaplitt, 2015), a detailed understanding of its physiological mechanisms is lacking.

The NAc consists of at least two subregions, a medial "shell" region and a more lateral "core" component associated with the extended amygdala and the basal ganglia, respectively (Zahm and Brog, 1992). The core and shell have different morphology and serve different cognitive functions (reward- and motivation-related learning, respectively; Floresco 2015; Salgado and Kaplitt 2015). The principal cell type is GABAergic projection medium-spiny neurons (MSNs) which express either D1 or D2 receptors and play specific roles in NAc-mediated behaviors and disorders (Lobo and Nestler, 2011; Francis et al., 2015).

In young mice, MSNs' intrinsic and synaptic properties diverge: D2 MSNs are more excitable than D1. Whether these specific differences in MSNs persist in adulthood remains unknown. NAc MSNs receive and integrate glutamatergic inputs, most notably from the prelimbic region of the prefrontal cortex (PFC), the ventral hippocampus (vHipp) and basolateral amygdala (BLA) (Groenewegen et al., 1999; Britt et al., 2012) but also from the thalamus, dorsal hippocampus, VTA and insular cortex (Stratford and Wirtshafter, 2013; Qi et al., 2016; Zhu et al., 2016; Trouche et al., 2018; Rogers-Carter et al., 2019). These regions process dissociable types of information and the specific activation of these pathways can elicit distinct behavioral functions via interactions with the NAc (Goto and Grace, 2008; Sesack and Grace, 2010). The PFC and the NAc interact in behaviors that require executive attention or working memory (Christakou et al., 2001, 2004; Cools et al., 2007), that place high demands on attention (Christakou et al., 2004), or necessitate the linking of behaviors across contexts (Floresco et al., 1999). The vHipp-NAc pathway is essential for spatial navigation in relation to goal direct behavior (Floresco et al., 1997; Ito et al., 2008; Mannella et al., 2013) and in encoding the temporal dynamics of decision making (Cardinal and Howes, 2005; Eichenbaum, 2014; Abela et al., 2015). By contrast, the BLA-NAc pathway plays a large role in conditioned emotional responses (Everitt et al., 2003;

LeDoux, 2003; Tye et al., 2011; Beyeler et al., 2016, 2018) and in forming associations between stimuli that predict appetitive or aversive consequences (Everitt et al., 1991; McLaughlin and Floresco, 2007; Shiflett and Balleine, 2010; Fernando et al., 2013).

The mesocorticolimbic endocannabinoid (eCB) system modulates a vast array of synaptic functions (Robbe et al., 2002; Lafourcade et al., 2007; Araque et al., 2017). eCB-mediated long-term depression was originally discovered in the NAc/ventral striatum (Robbe et al., 2002) and dorsal striatum (Gerdeman et al., 2002). eCB dysfunction is implicated as a major causal factor in a plethora of synaptopathies linked to the NAc (Kasanetz et al., 2010; Lafourcade et al., 2011; Jung et al., 2012; Neuhofer et al., 2015, 2018; Bosch-Bouju et al., 2016; Araque et al., 2017; Manduca et al., 2017). In the dorsal striatum, chemically induced eCB-synaptic plasticity shows pathway but not MSN subtype specificity (Wu et al., 2015). Whether eCBs contribute to pathway-specificity in the NAc and its mechanistic underpinnings is unknown. Here, we explored the innervation and synaptic properties of PFC, BLA and vHipp to the NAc core. In addition, we assayed each pathway for eCB receptors and dissected eCB-plasticity at BLA inputs. We report that adult D1- are inherently more excitable than D2 MSNs and that the hierarchy of excitatory inputs depends on the identity of the postsynaptic target MSN and on circuit specific properties. Finally, we provide evidence that the eCB system endows excitatory circuits of the NAc with pathway- and cell-specific plasticity. Together these data reveal a high degree of synapse and circuit specificity in the adult NAc core.

MATERIALS AND METHODS

Animals

Animals were treated in compliance with the European Communities Council Directive (86/609/EEC) and the United States National Institutes of Health Guide for the care and use of laboratory animals. The French Ethical committee authorized this project (APAFIS#3279-2015121715284829 v5). Male Drd1a-tdTomato mice were from The Jackson Laboratory (Bar Harbor, ME, USA) and female C57Bl/6J background mice were purchased from the Janvier Laboratory (Le Genest-Saint-Isle, France). Mice were acclimated to the animal facility for one week and then housed in male and female pairs to enable breeding of hemizygous offspring. Mice were ear punched for identification and genotyping. Mice were housed at constant room temperature (20 ± 1°C) and humidity (60%) and exposed to a light cycle of 12h light/dark (08:00 a.m. to 08:00 p.m.), with ad libitum access to food and water. All experiments were performed on male offspring C57BL/6J mice between P100 and P130.

Injection of the virus

Microinjection needles (32G) were connected to a 10 µL Hamilton syringe and filled with purified, concentrated adeno-associated virus (1.98x1013 infectious units per mL) encoding hChR2-EYFP under control of the CaMKIIα promoter (University of Pennsylvania, Philadelphia, USA). Mice were anesthetized with 150 mg/kg ketamine and 50 mg/kg xylazine and placed in a stereotaxic frame. Microinjection needles were bilaterally placed into the vHipp (Coordinates: AP=-3.2mm; ML=2.85mm; DV=3.84mm), basolateral amygdala (Coordinates: AP=-1mm; ML=3.1mm; DV=3.9mm) or prefrontal cortex (Coordinates: AP=2mm; ML=0.3mm; DV=2mm) and 250 nL virus was injected with a speed of 100 nL/min. The needles were left in place for an additional 5 min to allow for diffusion of virus particles away from injection site.

Slice preparation

Five to six weeks after surgery, adult male mice (P100-P130) were deeply anesthetized with isoflurane and sacrificed as previously described (Robbe et al., 2002; Lafourcade et al., 2011; Jung et al., 2012; Neuhofer et al., 2018). The brain was sliced (300 µm) on the coronal plane with a vibratome (Integraslice, Campden Instruments) in a sucrose-based solution at 4°C (in mm

as follows: 87 NaCl, 75 sucrose, 25 glucose, 2.5 KCl, 4 $MgCl_2$, 0.5 $CaCl_2$, 23 $NaHCO_3$ and 1.25 NaH_2PO_4). Immediately after cutting, slices containing the NAc were stored for 1 h at 32°C in a low calcium ACSF that contained (in mm) as follows: 130 NaCl, 11 glucose, 2.5 KCl, 2.4 $MgCl_2$, 1.2 $CaCl_2$, 23 $NaHCO_3$, 1.2 NaH2PO_4, and were equilibrated with 95% O2/5% CO2 and then at room temperature until the time of recording. EYFP expression was examined in slices containing the virus injection sites to assess placement accuracy.

Electrophysiology

Whole-cell patch-clamp recordings of visualized NAc medium spiny neurons (MSNs) were made in coronal slices containing the NAc as previously described (Robbe et al., 2002; Lafourcade et al., 2011; Jung et al., 2012; Neuhofer et al., 2018). During the recording, slices were placed in the recording chamber and superfused at 2 mL/min with normal ACSF. All experiments were done at 25°C. The superfusion medium contained picrotoxin (100 µM) to block GABA Type A (GABA-A) receptors, unless specified otherwise. All drugs were added at the final concentration to the superfusion medium.

For whole-cell patch-clamp experiments, neurons were visualized using an upright microscope with infrared illumination. The intracellular solution was based on K^+ gluconate (in mM as follows: 145 K^+ gluconate, 3 NaCl, 1 $MgCl_2$, 1 EGTA, 0.3 $CaCl_2$, 2 Na^+ATP, and 0.3 Na^+GTP, 0.2 cAMP, buffered with 10 HEPES). The pH was adjusted to 7.2 and osmolarity to 290-300 mOsm. Electrode resistance was 4-6 MOhm.

A -2 mV hyperpolarizing pulse was applied before each evoked EPSC to evaluate the access resistance, and those experiments in which this parameter changed >25% were rejected. Access resistance compensation was not used, and acceptable access resistance was <30 MOhm. The potential reference of the amplifier was adjusted to zero before breaking into the cell. Cells were held at -70 mV.

Current-voltage (I-V) curves were made by a series of hyperpolarizing to depolarizing current steps immediately after breaking into the cell. Membrane resistance was estimated from the I-V curve around resting membrane potential (Kasanetz et al., 2010; Thomazeau et al., 2014; Martin et al., 2017).

The paired-pulse ratio (PPR) was calculated from the peak current of two closely spaced EPSCs (50 ms), such that the PPR = Peak 2/Peak 1. Quoted PPR values are the average of 30 trials. For

the measurements of quantal EPSCs (qEPSCs), transmitter release was desynchronized by substituting calcium with strontium (4 mM) in the superfused ACSF. Asynchronous EPSCs were examined during a 200 ms window beginning 5 ms after optical stimulation. Recordings were analyzed if the frequency of events in this 200 ms window were significantly greater than during the 200 ms window preceding the stimulation as previously described (Britt et al., 2012).

Optogenetics

A 473 nm laser (Dragon Laser, Changchun Jilin, China) coupled to a 50 µm core glass silica optical fiber (ThorLabs) was positioned directly above the slice orientated at 30° approximately 350 µm from the recording electrode. At the site of recording discounting scattering a region of approximately 0.05 mm^2 was illuminated that after power attenuation due to adsorption and scattering in the tissue was calculated as approximately 100 mW/mm^2 (Yizhar et al., 2011). Optically evoked EPSCs were obtained every 10 s with pulses of 473 nm wavelength light (0-10 mW, 2 ms).

RNAscope ISH assay

Staining for Drd1, Drd2 and Trpv1 mRNAs was performed using single molecule fluorescent in situ hybridization (smFISH). Brains from 2 C57Bl/6J 8-week-old male mice were rapidly extracted and snap-frozen on dry ice and stored at -80°C until use. Ventral striatum coronal sections (14 µm) were collected directly onto Superfrost Plus slides (Fisherbrand). RNAscope Fluorescent Multiplex labeling kit (ACDBio Cat No. 320850) was used to perform the smFISH assay according to manufacturer's recommendations. Probes used for staining are mm-Trpv1-C1 (ACDBio Cat No. 313331), mm-Drd1-C2 (ACDBio Cat No. 461901-C2) and mm-Drd2-C3 (ACDBio Cat No. 406501-C3). After incubation with fluorescent-labeled probes, slides were counterstained with DAPI and mounted with ProLong Diamond Antifade mounting medium (Thermo Fisher scientific P36961). Fluorescent images of labeled cells in the NAc Core (Bregma 1.54 mm to 1.42 mm) were captured using sequential laser scanning confocal microscopy (Leica SP8).

Drugs

Drugs were added at the final concentration to the recording ACSF media. Picrotoxin, strontium, capsaicin and tetrodotoxin from Sigma (St. Quentin Fallavier, France); capsazepine and CP55,940 from Tocris Cookson (Bristol Bioscience, UK); CNQX and SR 141716 from the National Institute of Mental Health's Chemical Synthesis and Drug Supply Program (Rockville, MD, USA);

Data Acquisition and Analysis

Whole-cell patch-clamp recordings were performed with an Axopatch-200B amplifier as previously described (Robbe et al., 2002; Kasanetz and Manzoni, 2009; Lafourcade et al., 2011; Jung et al., 2012; Thomazeau et al., 2014, 2017; Martin et al., 2017). Data were low pass filtered at 2 kHz, digitized (10 kHz, DigiData 1440A, Axon Instruments), collected using Clampex 10.2 and analyzed using Clampfit 10.2 (all from Molecular Device). The magnitude of plasticity was calculated and compared 25-30 min after induction.

Spontaneous and quantal AMPAR-mediated EPSCs (sEPSCs/qEPSCs) were recorded using Axoscope 10 (Molecular Devices). sEPSCs/qEPSCs were filtered at 2 kHz and digitized at 20 kHz. sEPSCs/qEPSCs amplitude and frequency were analyzed with Axograph X using a double exponential template: $f(t)=\exp(-t/rise)+\exp(-t/decay)$, rise=0.5 ms. The threshold of amplitude detection was set at 5 pA.

Statistics

Statistical analysis of data was performed with Prism (GraphPad Software 6.0) using tests indicated in the main text after outlier subtraction (ROUT test). N values represent cells or individual animals. All values are given as mean ± SEM, and statistical significance was set at $*p < 0.05$.

RESULTS

We recorded a total of 412 medium spiny neurons (MSNs) from the NAc core of 291 *Tg (Drd1a*-tdTomato) Calak hemizygous adult male mice (P100-130). MSNs were either tdTomato-labeled "D1-positive" MSNs or tdTomato-unlabeled/presumably "D1-negative" MSNs. Because previous studies have consistently shown that unlabeled D1 negative MSNs are all D2 positive MSNs, in the remainder of the study we refer to tdTomato-unlabeled MSNs as D2 MSNs (Bertran-Gonzalez et al., 2008; Ade et al., 2011; Enoksson et al., 2012; Thibault et al., 2013; Cao et al., 2018).

Intrinsic properties of D1 and D2 medium spiny neurons in adult Drd1a-tdTomato mice

In juvenile and adolescent mice, D2 MSNs are more excitable than D1 MSNs in the NAc (Grueter et al., 2010; Ma et al., 2014; Cao et al., 2018). To our knowledge, the intrinsic properties of D1 and D2 MSNs in adult NAc core have not previously been described.

The intrinsic properties of current-clamped and visually identified neighboring D1 and D2 MSNs were compared in NAc core slices from adult *Drd1a*-tdTomato mice **(Figure 1)**. The membrane reaction profiles of D1 and D2 MSNs in response to a series of somatic current steps differ greatly **(Figure 1B)**. Differences between MSN subtypes extended to their resting membrane potential which was significantly more depolarized in D1 than D2 MSNs **(Figure 1C)** and the rheobase was significantly lower in D1 than D2 MSNs **(Figure 1D)**. The "hyper-excitability" of D1 MSNs was accompanied by an increased number of action potentials in response to somatic currents steps in D1 compared to D2 MSNs **(Figure 1E)**. Action potential duration was also shorter in D1 MSNs and action potential after-hyperpolarization (fAHP) was larger in D2 MSNs **(Figure 1F-L)**. Thus, in the NAc core of adult mice, D1 MSNs are more excitable than D2 MSNs.

Cell-type specific hierarchy of excitatory inputs in the adult NAc core

In postsynaptic NAc shell MSNs, optogenetic methods and targeted channelrhodopsin-2 (ChR2) expression to projection neurons from the ventral hippocampus (vHipp), basolateral amygdala (BLA) and prefrontal cortex (PFC) revealed that vHipp inputs elicit the largest excitatory currents (vHipp>BLA>PFC; Britt et al., 2012). At the strict anatomical level, the PFC

preferentially projects to the NAc core, in contrast with the vHipp which preferentially projects to the shell. The BLA projects equally to both NAc core and shell (Li et al., 2018).

However, the functional hierarchy of specific excitatory synaptic inputs to identified MSN subtypes in the NAc core is largely unknown. Akin to Britt and collaborators (Britt et al., 2012), we targeted ChR2 expression to projection neurons in the vHipp, BLA and PFC in order to compare the functional strength and synaptic properties of these inputs onto identified D1 and D2 MSNs in the NAc core of adult mice.

Five to six weeks after viral infection with pAAV9-CaMKIIa-hChR2(H134R)-EYFP in the vHipp, BLA or PFC, strong expression of ChR2-EYFP was observed in the NAc core **(Figure 2A)**. To best mimic "real life" action potentials and avoid direct illumination of axon terminals, light pulses (473nm) were delivered with a custom-made optical fiber placed approximately 350 µm from the recorded MSNs **(Figure 2B)**. Independently of input, light-evoked excitatory postsynaptic currents ("optical EPSCs", oEPSCs) were abolished in the presence of the ionotropic glutamate receptor antagonist CNQX (20 µM) or the sodium channel blocker tetrodotoxin (TTX, 1 µM) **(Figure 2C)**. These control experiments show that oEPSCs are genuinely glutamate-mediated EPSCs induced following light-evoked activation of axonal Na^+ channels.

In the NAc shell, "irrespective of which pathway was optically stimulated, oEPSCs were observed in more than 95% of recorded neurons" (Britt et al., 2012). In our experiments the same held true (data not shown), irrespective of MSN subtypes, suggesting that each MSN receives innervation from PFC, vHipp and BLA (Finch, 1996; Groenewegen et al., 1999; French and Totterdell, 2002, 2003; McGinty and Grace, 2009; Britt et al., 2012).

Using increasing optical stimulations and whole-cell patch clamp of visually identified MSNs, we built and compared input-output curves for PFC, BLA and vHipp inputs at both D1 and D2 MSNs **(Figure 3, see also Figure 6)**. We compared evoked oEPSCs in response to increasing stimulation intensity in different pathways across D1 and D2 MSNs **(Figure 3)**. We found that, when excitatory currents were elicited by optical stimulation of PFC fibers, the largest oEPSCs were observed at D2 MSNs (**Figure 3A-D**). Similar experiments performed at BLA and vHipp inputs showed that BLA-D1 > BLA-D2 (**Figure 3B-E**) and vHipp-D2 > vHipp-D1 (**Figure 3C-F**). These data show that in the adult NAc core, the hierarchy of synaptic inputs is specific to the cellular identity of the target MSNs.

Input- and cell-type-specific drive of action potential firing in the adult NAc core

What is the relationship between maximal excitatory synaptic strength and action potential firing of identified MSNs? We first sought to determine if the pathway/cell specificity extended to the ability of different pathways to drive postsynaptic action potentials in identified MSNs. Current-clamp recordings revealed that optical recruitment of PFC inputs elicited postsynaptic action potentials with greater probability in D2 than D1 MSNs (**Figure 4A**). In marked contrast, BLA inputs onto D1 MSNs were more likely to trigger action potentials than those onto D2 MSNs **(Figure 4B)**. Finally, there was no difference at vHipp inputs **(Figure 4C)**. Performed in the absence of inhibition, i.e. in the presence of picrotoxin, these results faithfully mirror the aforementioned cell-type specificity of the hierarchy of synaptic strength.

Input- and cell-type-specific synaptic properties in the adult NAc core

To investigate cell-type specific connectivity at glutamatergic inputs into the NAc, we compared post- and pre-synaptic parameters at disambiguated synapses in the NAc core. First, we measured the paired-pulse ratio (PPR), a classical index of neurotransmitter release probability (Silver et al., 1998) **(Figure 5A,B)**. In D1 MSNs, BLA inputs had a low PPR/high release probability and the highest PPR/lowest release probability was found at PFC inputs (D1: BLA>vHipp>PFC). In contrast, in D2 MSNs, PFC inputs exhibited the highest release probability, respectively, while the lowest probability of release was found at BLA inputs (D2: PFC=vHipp>BLA).

In immature mice, miniature EPSCs properties were similar in D1 and D2 MSNs in early life (P16-24, Cao et al., 2018), while around P42 spontaneous EPSCs (sEPSCs) are more frequent in D2 MSNs (Ma et al., 2012) in disagreement with an earlier report of higher miniature EPSCs in D1 MSNs (P28-56, Grueter et al., 2010). We recorded sEPSCs in D1 and D2 NAc core MSNs of adult mice **(Figure 5C,D)**. The amplitude of the sEPSCs measured in D1 MSNs was slightly larger than that measured in D2 MSNs (in agreement with Grueter et al., 2010). Both MSN subtypes exhibited similar distribution and average inter-event intervals.

Next, we measured light-evoked input-specific quantal EPSCs (qoEPSCs) by replacing our extracellular medium's calcium with strontium to desynchronize transmitter release (Britt et al., 2012; McGarry and Carter, 2017). qoEPSC amplitude provides a direct estimate of postsynaptic

efficacy measure and qoEPSC frequency was taken as an indirect indication of the number of connections (Goda and Stevens, 1994).

At PFC and vHipp inputs, qoEPSC frequencies were similar across cell types (**Figure 5E-F**). However, qoEPSC frequencies were larger at BLA-D2 than BLA-D1 synapses (**Figure 5G-H**). In contrast, qoEPSC amplitude were larger at PFC-D1 and BLA-D2 synapses compared to the other afferents (**Figure 5G-H**).

The large qoEPSC frequency and amplitude observed at BLA-D2 synapses may at first appear to be at odds with the high PPR/release probability at these synapses as estimated by our input/output experiments **(Figure 3)**. Although asynchronous events are considered "calcium-independent" (i.e. no calcium is present), strontium desynchronization is most likely the result of strontium's low-affinity binding to the calcium sensor underlying excitation/secretion coupling. Thus, differences in calcium-dependent processes in the terminals (e.g. posttranslational modification) may account for the difference between these two techniques. Another cautious interpretation of the results is that high quantal size and low Pr combine to yield a "weak" synapse.

Pathway specific expression of CB1R and TRPV1R receptors

The endogenous cannabinoid (eCB) system modulates synaptic circuits in the CNS and notably the dorsal and ventral striatum (Araque et al., 2017). Inhibitory CB1 receptors (CB1R) have long been described at glutamatergic NAc core synapses using standard electrical stimulation (Robbe et al., 2001). Stimulation of CB1R with a submaximal dose of a synthetic cannabimimetic (CP55940 1µM, **Figure 6A, B**) inhibited oEPSC in D1 and D2 MSNs irrespective of the input pathway, in support of the idea that functional CB1R are present at all of these inputs. The degree of inhibition induced by the single dose used here, however, was pathway dependent. Thus, CP55940-induced inhibition was larger at BLA than PFC or vHipp-D1 synapses (**Figure 6C)** and smaller at vHipp-D2 synapses (compared to PFC and BLA, **Figure 6D**).

The nonselective cation channel, transient receptor potential cation channel subfamily V member 1 (TRPV1R), is a multifaceted mediator of eCB signaling in the CNS (Gibson et al., 2008; Manduca et al., 2017; Bara et al., 2018), notably in the striatum: pharmacological activation of TRPV1R suppresses and facilitates transmitter release in the dorsal striatum (Musella et al., 2009) and inhibits excitatory inputs onto D2 NAc core MSNs (Grueter et al., 2010). Multiple

353 inputs onto D1 and D2 MSNs differentially expressing various levels of TRPV1R could explain
354 these apparently contradicting results. Thus, we compared the effects of the specific TRPV1R
355 agonist capsaicin in the disambiguated NAc core synapse preparation **(Figure 7)**. While
356 capsaicin inhibited PFC-evoked oEPSCs in both D1 and D2 MSNs **(Figure 7A-B, left panels)**, the
357 TRPV1R agonist had multi-faceted effects on the other pathways. Capsaicin had opposite
358 effects on BLA-evoked oEPSCs depending on the MSNs' subtypes: the efficacy of BLA D1 MSN
359 synapses was enhanced in the presence of the TRPV1 agonist but reduced at BLA-D2 MSNs
360 synapses **(Figure 7A-B, middle panels)**. Finally, at vHipp inputs, TRPV1R activation specifically
361 inhibited vHipp-D1 synapses and had no effect at vHipp synapses onto D2 MSNs **(Figure 7A-B,**
362 **right panels)**. These results are summarized **Figure 7-D**.
363 At excitatory inputs in the NAc core, CB1R are expressed presynaptically (Robbe et al., 2001;
364 Micale et al., 2009) and mediate presynaptic retrograde LTD (Robbe et al., 2002) while TRPV1R
365 are localized postsynaptically (Micale et al., 2009) and trigger postsynaptic LTD specifically in D2
366 MSNs (Grueter et al., 2010; Neuhofer et al., 2018). We combined electrophysiological and
367 RNAscope approaches to identify TRPV1R's loci of expression in our model. Capsaicin had
368 opposite effects on spontaneous' EPSCs recorded in D1 and D2 MSNs. In D1 MSNs the TRPV1R
369 agonist reduced the frequency of spontaneous EPSCs **(Figure 8A)**, but not their amplitude, in
370 support of a presynaptic localization **(Figure 8B)**. In D2 MSNs however, capsaicin reduced the
371 amplitude of spontaneous EPSCs **(Figure 8B),** but not their frequency **(Figure 8A),** in support of
372 a postsynaptic localization. These functional observations were corroborated by the
373 distribution of *Trpv1*, *Drd1* and *Drd2* mRNAs. Triple staining indicated that in the NAc Core,
374 *Trpv1* mRNA was preferentially enriched in D2 MSNs compared to D1 expressing MSNs **(Figure**
375 **8C)**.
376 Taken together, these results reveal that while CB1R are uniformly expressed across input
377 pathways onto D1/D2 MSNs, TRPV1R modulate excitatory inputs to the NAc core in a pathway-
378 and cell-type specific manner.
379
380 **Cell-type specific endocannabinoid-mediated LTD at amygdala synapses**
381 In the last series of experiments, we focused on the BLA-NAc core synapses. These synapses are
382 instrumental to reward-seeking behavior (Ambroggi et al., 2008) and have a role in positive
383 emotional valence (Beyeler et al., 2018). Our present observation that both TRPV1R and CB1R

modulate synaptic transmission in a cell-type specific manner raised the possibility that the eCB interplay controls the polarity of activity-dependent plasticity at BLA-NAc synapses.

In the striatum, the principal form of eCB-mediated synaptic plasticity is LTD (Robbe et al., 2002; Gerdeman et al., 2002). We first compared the expression of eCB-LTD at BLA-D1 and -D2 synapses. Using the canonical protocol that elicits eCB-LTD in NAc MSNs (Robbe et al., 2002), we observed a robust LTD in D2 but not D1 MSNs following optical stimulation **(Figure 9)**. This is, to our knowledge, the first evidence that eCB-LTD can be optogenetically-induced at a single set of identified synapses. While this experiment can be interpreted as a lack of eCB-LTD at BLA inputs onto D1 MSNs, the current pharmacological characterization and previous work in the NAc core (Neuhofer et al., 2018) led us to test the possibility of another, more complex scenario. Based on the enhancing effects of the TRPV1R agonist at BLA-D1 synapses, we hypothesized that tetanus-induced eCB release (presumably anandamide) and the ensuing potentiation masked/prevented the induction of LTD. In support of this idea we observed that in the presence of a TRPV1R antagonist (capsazepine, CPZ 10 µM) the otherwise inefficacious protocol triggered a large LTD **(Figure 9C-D)**. Interestingly, bath application of the CB1R antagonist SR 141716 (5 µM) prevented the induction of LTD in the presence of CPZ **(Figure 9C-D)**.

The mirror situation was observed at BLA-D2 synapses. There, LTD was converted to LTP in the presence of the TRPV1R antagonist **(Figure 9E-F)**, a result compatible with the current finding that TRPV1R are inhibitory on BLA-D2 synapses **(Figure 9)**. We finally controlled for the role of CB1R in BLA-D2 LTD. Bath-application of the SR 141716 (5 µM) blocked post-tetanic depression and prevented LTD **(Figure 9E-F)** showing that CB1R-mediate BLA-D2 LTD.

DISCUSSION

Our principal findings are that in the adult mouse NAc core, 1/ the hierarchy of excitatory inputs depends on the identity of the postsynaptic target MSN and on circuit specific properties and 2/ the eCB system endows excitatory circuits of the NAc with pathway-specific plasticity.

Differential intrinsic properties of adult NAc core MSNs

The data show that D1 and D2 MSNs in adult NAc core have distinctive intrinsic properties. Compared to D2, D1 MSNs had a low rheobase, a more depolarized membrane potential and exhibited a higher propensity to trigger action potentials in response to depolarizing current injections. Thus, adult D1 are more excitable than D2 MSNs.

Subtype specific morphological properties (e.g. soma size or dendritic arborization, Gertler et al., 2008) and differences in membrane biophysical properties such as membrane resistance, capacitance, or the expression of voltage dependent calcium channels, may explain these dissimilarities (Nisenbaum et al., 1994; Hernández-López et al., 1997, 2000).

Divergent intrinsic properties have already been described in juvenile and adolescent mice, however, at these stages D2- are more excitable than D1-MSNs (Kreitzer and Malenka, 2007; Gertler et al., 2008; Ma et al., 2012; Planert et al., 2013; Cao et al., 2018). While many factors (e.g. recording site, sample size, the presence or absence of TTX, the transgenic mouse line used, the size of the soma or the extent of dendritic arborization) may explain this discrepancy, it is highly probable that age is the determining factor. In keeping with this idea, in rat NAc core, prepubertal rats and adult rats display different properties (Belleau and Warren, 2000; Zhang and Warren, 2008; Kasanetz and Manzoni, 2009). Additionally, in both rats and mice, NAc dopamine receptors undergo significant developmental changes during adolescence (Andersen et al., 1997; Andersen and Teicher, 2000).

The subtype specific evolution of excitability in juvenile/adolescent and adults MSNs may be due to differences in membrane resistance and conductance. In support of this possibility, early in development MSNs have very high membrane resistance and do not express inward rectifying potassium channels (Tepper et al., 1998; Belleau and Warren, 2000). The time-scale of this physiological maturation parallels the morphological development of MSNs and

dendritic arborization, spine formation and synaptogenesis which continue until the end of the first postnatal month (Tepper et al., 1998; Butler et al., 1999).

The hierarchy of excitatory afferents depends on MSNs' subtype in adult NAc core

Pathway-specific opto-stimulation of excitatory inputs in the NAc core revealed that there is a hierarchy of synaptic inputs that depends on the cellular identity of the target MSNs. Most notably, the BLA and the PFC are the main source of synaptic excitation on D1 and D2 neurons, respectively. Similarly, BLA and PFC afferents trigger action potentials with a high probability in D1 and D2 MSNs, respectively.

Differences in the number of fibers per afferent or the amount of glutamate release per fibers may underlie this functional hierarchy. Based on the recent study of Li and colleagues (Li et al., 2018) that showed similar PFC, BLA and vHipp innervations of D1 and D2 MSNs, we favor the second proposition.

Input and synapse specific function of endocannabinoids

The present data indicate that functional CB1R are present at all synapses tested, albeit with differences in the amount of CB1R-mediated inhibition. The situation was far more complex with TRPV1R. Indeed, a TRPV1R agonist inhibited PFC-evoked oEPSCs in both D1 and D2 MSNs but led to opposite and MSN subtype-specific effects at the BLA pathway: BLA-D1 were enhanced while BLA-D2 synapses were inhibited by capsaicin. TRPV1R specifically inhibited vHipp-D1 synapses and had no effect on vHipp-D2 synapses. Pharmacological activation of TRPV1R suppresses or facilitates neurotransmitter release into the dorsal striatum according to their pre- or postsynaptic location (Musella et al., 2009) and our results with sEPSCs also suggest a differential expression of TRPV1R at BLA-D1 and BLA-D2 synapses. Indeed, capsaicin modified the frequency but not the amplitude of sEPSCs in D1 MSNs and vice-versa in D2 MSNs. These data are compatible with presynaptic TRPV1R at BLA-D1 and postsynaptic TRPV1R at BLA-D2 synapses. Of note, Grueter et al. also reported a postsynaptic localization of TRPV1R at D2 MSNs (Grueter et al., 2010).

At the BLA-NAc pathway, TRPV1R and CB1R modulate synaptic transmission in a cell specific manner: LTD could be induced in D2 but not in D1 MSNs in agreement with a previous report where the identity of MSNs was not ascertained (Grueter et al., 2010). At first glance, these

results may be taken as an indication that BLA-D2 MSNs are incapable of expressing eCB-LTD. However, the current pharmacological characterization and previous work (Neuhofer et al., 2018) led us to hypothesize that the tetanus-induced eCB (presumably anandamide) activates TRPV1R and that the ensuing potentiation masked/prevented LTD. In support of this idea, we observed that, in the presence of a TRPV1R antagonist, the previously inefficient protocol triggered a large LTD. The mirror situation was observed at BLA-D2 synapses where LTD was converted to LTP in the presence of the TRPV1R antagonist.

In summary, our study reveals the cell-type- specific synaptic organization of hippocampal, amygdala and prefrontal inputs to the PFC. It is tempting to speculate that pathway and cell specific synaptic strengths correlate with distinct functions and associated behaviors. Future work will determine if the PFC-D2 “dominant pathway” is preferentially engaged in executive functions and the role of the BLA-D1 pathway in emotional behaviors. In this context, the observation that two subpopulations of BLA glutamatergic neurons project to NAc core D1 or D2 MSNs to generate emotional responses of opposite valence is an indication of similar parallel dual control circuits at PFC- and/or vHipp-NAc pathways (Shen et al., 2019).

Moreover, these data highlight the versatility of the endocannabinoid system in shaping activity-dependent synaptic plasticity at BLA-NAc circuits and cortical-limbic circuits in general.

In conclusion, our experiments reveal a high degree of synapse and circuit specificity in the adult NAc core and illustrate how endocannabinoids contribute to pathway-specific synaptic plasticity.

LEGENDS:

Figure 1: Adult NAc core D1 MSNs are more excitable than D2 MSNs

A) Typical membrane responses from NAc core D1 or D2 MSNs in reaction to a series of increasing somatic current injections. Sample spike trains in response to depolarizing current from D1 or D2 MSN. **B)** Summary of all the current-voltage (I-V) curves recorded in D1 (black, n=30) and D2 (white, n=26) MSNs ($F_{(interaction\ 26,1404)}$=8.03, p<0.0001, $F_{(cell\ type\ 1,54)}$=2.893, p<0.0001, two-way repeated measures ANOVA). **C)** The resting membrane potential of D2 MSNS was significantly hyperpolarized compared to that of D1 MSNs (p=0.0051, Mann-Whitney U test). **D)** The rheobase, the minimal current required to trigger an action potential, was much lower in D1 MSNs (p=0.0025, Mann-Whitney U test). **E)** The number of evoked action potentials in response to increasing depolarizing current steps was larger in D1 MSNs compared to D2 MSNs ($F_{(interaction\ 12,648)}$= 5.927, p<0.0001, $F_{(cell\ type\ 1,54)}$=27.38, p<0.0001, two-way repeated measure ANOVA). **F)** Example of individual AP evoked by depolarizing current injection, indicating delay to the first spike, AP threshold, AP amplitude, AP duration, fAHP amplitude and fAHP duration metrics. **G)** AP duration is shorter in D1 MSNs compared to D2 MSNs (D1 MSNs n=30; D2 MSNs n=26, p=0.0354, Mann-Whitney U test). The following action potential properties did not vary between the MSN subtype: **H)** delay to the first spike, **I)** AP threshold, **J)** AP amplitude and **K)** fAHP amplitude. **L)** fAHP duration is increased in D2 MSNs compared to D1 MSNs (p=0.0009 Mann-Whitney U test). Individual point in scatter dot plots represents one individual neuron. All values are represented as mean ± SEM. *p<0.05.

Figure 2: Pathway specific evoked excitatory postsynaptic currents (EPSCs) in the Nac core following optical stimulation of ventral hippocampal, basal amygdala or prefrontal cortex inputs

A) Representative coronal brain slices showing expression of ChR2-eYFP (green) following injections of (0.25 µL) AAV9.CamKIIa.hChR2(H134R)-eYFP.WPRE.hGH (Addgene26969P; 1.98 x 10 GC/mL)) in the ventral hippocampus (vHipp), basolateral amygdala (BLA) or prefrontal cortex (PFC) (left). Image of ChR2-EYFP expressing axons from principal (i.e. CamKII expressing) cortical neurons (right). **B)** Illustration of the experimental set up. Synaptic terminals expressing ChR2-EYFP were stimulated with a 473 nm laser coupled to an optical fiber placed 350 µm from the

recording area. Recordings of Optically evoked EPSCs were recorded in the whole-cell patch-clamp configuration in medium spiny neurons (MSNs) from the NAc core. **C)** Inward currents evoke by light stimulation in NAc core MSNs. CNQX (20 µM) and TTX (1 µM) completely prevented evoked currents recorded in the presence of PTX following optical stimulation of PFC inputs, showing that the oEPSCs depended on presynaptic and post-synaptic glutamate ionotropic AMPAR receptor-mediated currents. Individual oEPSCs amplitude experiments before (pre) and after CNQX (n=10) or TTX (n=9). Blue dots indicate optical stimulations. **D-E)** Location of whole-cell patch-clamped MSNs sorted by subtype in nucleus NAc core of Drd1-tdTomato transgenic mice. "D1" represent recordings from fluorescently labeled D1-positive MSNs **(D)** and "D2" from non-fluorescently labeled MSNs **(E)**.

Figure 3: The hierarchy of optically driven synaptic inputs depends on the cellular identity of the target MSNs

A) Left, at PFC fibers the largest excitatory oEPSCs in response to increasing light stimulations were recorded in D2 MSNs (light blue, n=17) compared to D1 MSNs (dark blue, n=11) ($F_{(interaction\ 15,416)}$= 18.59, p<0.0001, $F_{(cell\ type\ 1,416)}$= 934.4, p<0.0001, two-way repeated measure ANOVA). Right, example oEPSC traces for PFC inputs onto D1 and D2 MSNs. **B)** Left, at BLA fibers the largest excitatory oEPSCs in response to increasing light stimulations were recorded in D1 MSNs (dark green, n=20) compared to D2 MSNs (light green, n=15) ($F_{(interaction\ 15,528)}$= 5.628, p<0.0001, $F_{(cell\ type\ 1,528)}$= 331.5), p<0.0001, two-way repeated measure ANOVA). Right, example oEPSC traces for BLA inputs onto D1 and D2 MSNs. **C)** Left, at vHipp fibers the largest excitatory oEPSCs in response to increasing light stimulations were recorded in D2 MSNs (light orange, n=22) compared to D1 MSNs (dark orange, n=24) ($F_{(interaction\ 15,704)}$= 4.310, p<0.0001, $F_{(cell\ type\ 1,704)}$= 491.3, p<0.0001, two-way repeated measure ANOVA). Right, example oEPSC traces for vHipp inputs onto D1 and D2 MSNs. **D)** Summary bar histogram showing maximum oEPSCs at PFC inputs onto D1 and D2 MSNs. (D1 MSNs n=11, D2 MSNs n=11, p<0.0001, Mann-Whitney U test). **E)** Summary bar histogram of maximum oEPSCs at BLA inputs in neighboring D1 and D2 MSNs (D1 MSNs n=15, D2 MSNs n=15, p<0.0001, Mann-Whitney U test). **F)** Summary bar histogram of maximum oEPSCs at vHipp inputs in neighboring D1 and D2 MSNs neighboring (D1 MSNs n=22, D2 MSNs n=22, p<0.0001, Mann-Whitney U test). Individual point in scatter dot plots represents one individual neuron. The line between dots shows neighboring D1 and D2

552 neurons that were recorded in the same slice with the same optical fiber position. All values are
553 represented as mean ± SEM or geometric mean ± CI. *p<0.05.

554 **Figure 4: Pathway-specific drive of action potential in identified NAc core MSNs**
555 **A)** Left, comparison of the probability of AP firing versus pulse number shows that PFC inputs
556 preferentially drive the firing of D2 MSNs compared to D1 MSNs (D1 MSNs n=6, D2 MSNs n=6,
557 pulse 1: p=0.0005, pulse 2-5: p<0.0001, Fisher's exact test). Right, example traces of APs evoked
558 in D1 and D2 MSNs in response to trains of optical stimulation of PFC inputs (2 ms light pulses, 5
559 pulses at 10 Hz). **B)** Left, comparison of the probability of AP firing versus pulse number shows
560 that BLA inputs preferentially drive the firing of D1 MSNs compared to D2 MSNs (D1 MSNs n=7,
561 D2 MSNs n=6, pulse 1-3: p<0.0001, pulse 4: p=0.0027, pulse 5: p=0.0445, Fisher's exact test).
562 Right, example traces of APs evoked in D1 and D2 MSNs in response to trains of optical
563 stimulation of BLA inputs. **C)** Left, comparison of the probability of AP firing versus pulse
564 number shows no difference at vHipp inputs of the firing of D1 MSNs and D2 MSNs (D1 MSNs
565 n=6, D2 MSNs n=6, pulse 1: p=0.0357, pulse 2: p=0.1997, pulse 3-5: p=1.0000, Fisher's exact
566 test). Right, example traces of APs evoked in D1 and D2 MSNs in response to trains of optical
567 stimulation of vHipp inputs. Blue dots indicate time of stimulation. All experiments performed
568 in the presence of picrotoxin to prevent from feedforward inhibition. All values are represented
569 as mean ± SEM or geometric mean ± CI. *p<0.05
570
571 **Figure 5: Input- and cell-type-specific post and presynaptic properties in the NAc core**
572 **A)** Average paired-pulse ratio (P2/P1) measured in D1 and D2 MSNs (voltage-clamp, -70 mV) in
573 response to paired optical stimulations (50 msec interval) of PFC, BLA and vHipp inputs. PFC
574 inputs had a lower PPR/high release probability in D2 MSNs (light blue) compared to D1 MSNs
575 (dark blue) (D1 MSNs n=12, D2 MSNs n=19, p=0.0006, Mann-Whitney U test). BLA inputs had a
576 lower PPR/high release probability in D1 MSNs (dark green) compared to D2 MSNs (light green)
577 (D1 MSNs n=16, D2 MSNs n=18, p<0.0001, Mann-Whitney U test). vHipp inputs exhibited
578 similar release probability in both D1 (dark orange) and D2 MSNs (light orange) (vHipp: D1
579 MSNs n=15, D2 MSNs n=11, p>0.9999, Mann-Whitney U test). **B)** Example traces of evoked
580 paired oEPSC responses to optical stimulations of PFC, BLA and vHipp inputs recorded in D1
581 MSNs and D2 MSNs. **C)** Cell-type-specific differences in amplitude of sEPSCs in adult core MSNs:
582 Representative traces of whole-cell voltage clamp recording AMPAR event sEPSC from in D1

and D2 MSNs. **D)** Left, Cumulative probability plot of measured sEPSC event amplitudes. Summary bar chart shows mean AMPAR event sEPSC amplitude (D1 MSNs: n=32; D2 MSNs: n=26, p=0.0146, Mann-Whitney U test). Right, Cumulative probability plot of interval between measured sEPSC events. Scatter dot plots represents one cell. Summary bar chart shows mean AMPAR event sEPSC interval. **E)** Light-evoked input-specific quantal EPSCs (qoEPSC) in the adult NAc. At BLA inputs, qoEPSCs frequencies were larger in D2 MSNs compared to D1 MSNs (D1 MSNs n=6, D2 MSNs n=7, p=0.0734, Mann-Whitney U test). At PFC and vHipp inputs, qoEPSCs frequencies were similar in D1 MSNs and D2 MSNs (PFC: D1 MSNs n=7, D2 MSNs n=6, p=0.0361; vHipp: D1 MSNs n=6, D2 MSNs n=6, p=0.1429, Mann-Whitney U test). **F)** Representative qoEPSCs recorded in D1 MSNs and D2 MSNs in response to pathway specific opto-stimulation (arrows indicate detected qoEPSCs). **G)** At PFC inputs, qoEPSCs amplitudes were larger in D1 MSNs compared to D2 MSNs (D1 MSNs n=7, D2 MSNs n=6, p=0.0350, Mann-Whitney U test). At BLA inputs, qoEPSCs amplitudes were larger in D2 MSNs compared to D1 MSNs (D1 MSNs n=6, D2 MSNs n=7, p=0.0012, Mann-Whitney U test). At vHipp inputs, qoEPSC amplitudes were similar in D1 MSNs and D2 MSNs (D1 MSNs n=6, D2 MSNs n=6, p=0.1429, Mann-Whitney U test). **H)** Histograms for representative D1 cells and D2 cells showing the distribution of qoEPSC amplitude across all trials. Blue dots indicate optical stimulations. Individual point in scatter dot plots represents one individual neuron. All values are represented as mean ± SEM. *p<0.05.

Figure 6: CB1R inhibition is common to all inputs onto D1 and D2 NAc core MSNs

A) Bath application of the synthetic CB1R agonist CP55940 (1 µM), inhibited oEPSC in D1 (black) and D2 (white) MSNs. CP55940 was applied for 30 min (black bar) after at least 10 min of stable baseline recording. **B)** Individual and averaged oEPSCs amplitude experiments before (baseline) and 25-30 min after CP55940. (D1 MSNs, black circles: PFC n= 3, p=0.0014, BLA n=4, p=0.0110, vHipp n=3, p=0.0411; D2 MSNs, white circles: PFC n=4, p=0.0114, BLA n=4, p=0.0188, vHipp n=4, p=0.0496 paired t-test). **C)** Summary bar histogram comparing CP55940-induced inhibition of oEPSCs at identified PFC, BLA and vHipp inputs onto D1 (PFC n= 3, BLA n=4, vHipp n=3, $F_{(input\ 2,7)}$=14.32, p=0.0034, one-way ANOVA) and D2 MSNs (PFC n=4, BLA n=4, vHipp n=4, $F_{(input\ 2,9)}$=4.207, p=0.0513, one-way ANOVA). **D)** Schematic view of the relative weight of CB1R-

mediated inhibition at PFC, BLA and vHipp inputs onto D1 and D2 MSNs. n represents the number of mice. All values are represented as mean ± SEM. * p<0.05.

Figure 7: Divergent input and cell specific control of excitatory NAc synapses by TRPV1R

A) Effects of the TRPV1R agonist capsaicin (10µM) on oEPSCs at PFC, BLA and vHipp synapses onto D1 (black circles) and D2 (white circles) MSNs. Capsaicin was applied for 30 min (black bar) after at least 10 min baseline recording. Capsaicin inhibited PFC-evoked oEPSCs similarly in both D1 (black) and D2 (white) MSNs. Capsaicin enhanced BLA-D1 MSN synapses but inhibited BLA-D2 MSN synapses. Finally, capsaicin inhibited vHipp-D1 MSN synapses and has no effect at vHipp-D2 MSN synapses. **B)** Individual and averaged oEPSCs amplitude experiments 10 min before (baseline) and 25-30 min after capsaicin; D1 MSNs, black circles: PFC n= 3, p=0.0308, BLA n=4, p=0.0188, vHipp n=5, p=0.0010; D2 MSNs, white circles: PFC n=3, p=0.0135, BLA n=3, p=0.0087, vHipp n=3, p=0.0109 paired t-test). **C)** Summary bar histogram of the maximal effects of Capsaicin on oEPSCs at identified inputs onto D1 (PFC n= 3, BLA n=4, vHipp n=5, $F_{(input\ 2,9)}$=157.4, p<0.0001, one-way ANOVA) and D2 MSNs (PFC n=3, BLA n=3, vHipp n=3, $F_{(input\ 2,6)}$=8.586, p=0.0174, one-way ANOVA). **D)** Schematic view of the relative weight and effects of TRPV1R on oEPSCs at PFC, BLA and vHipp inputs onto D1 and D2 MSNs. n represents the number of mice. All values are represented as mean ± SEM, * p<0.05.

Figure 8: MSN-subtype selective expression and function of TRPV1R in the NAc core.

A) Left, capsaicin reduces the frequency of sEPSC and in D1 but not D2 MSNs. Summary bar histogram comparing the mean sEPSC frequencies in D1 (black, n=7) and D2 (white, n=6) MSNs before and after capsaicin (10µM). Right, individual and averaged sEPSCs frequency experiments before (Pre) and 25-30 min after capsaicin (D1 MSNs black circles, p=0.0013 paired t-test; D2 MSNs white circles p=0.1152 paired t-test). **B)** Left, capsaicin reduces the amplitude of sEPSC in but not D1 MSNs. Summary bar histogram comparing the mean sEPSC amplitudes in D1 (black, n=7) and D2 (white, n=6) MSNs before and after capsaicin. Right, individual and averaged sEPSCs amplitude (D) experiments before (Pre) and 25-30 min after capsaicin (D1 MSNs black circles, p=0.0559 paired t-test; D2 MSNs white circles p=0.0008 paired t-test). All values are represented as mean ± SEM, * p<0.05 paired t-test. **C)** Single-molecular fluorescent in situ hybridization for *Drd1* (blue), *Drd2* (green) and *Trpv1* (red) mRNAs in the NAc core. Slides

643 were counterstained with DAPI (white). Scale bar: 12 µm. Note the segregation of cells
644 expressing *Drd1* and *Drd2* mRNAs and the enrichment of *Trpv1* mRNA in D2 MSNs.
645
646 **Figure 9: TRPV1R delineates cell type-specific LTD at amygdala synapses in the NAc core**
647 **A)** Optical stimulation of BLA inputs (10 Hz for 10 min) induced a robust LTD in D2 (white circles,
648 n=4) but not in D1 MSNs (black circles, n=5). **B)** Individual and averaged oEPSC amplitude
649 before (baseline) and 25-30 min after LTD induction (LTD) in D1 and D2 MSNs (D1 MSNs,
650 p=0.3311, D2 MSNs, p=0.0072, paired t-test). **C)** Bath perfusion of the TRPV1R capsazepine (CPZ
651 10 µM) allowed the induction of LTD at BLA-D1 synapses (purple, n=6; compared to control
652 same as A). When CPZ was applied in the presence of the CB1R antagonist SR141716 (SR 5 µM)
653 LTD induction was prevented (orange, n=4). **D)** Individual and averaged oEPSCs amplitude
654 before (baseline) and 25-30 min after LTD induction (LTD) in D1 MSNs in control, CPZ and CPZ +
655 SR (D1 CPZ, p=0.0056 paired t-test; D1 CPZ + SR, p=0.9737). **E)** Antagonism of TRPV1R
656 converted LTD to LTP at BLA-D2 synapses (purple, n=5). Bath application of the CB1R antagonist
657 SR blocked LTD at BLA-D2 synapses (blue, n=6). **F)** Individual and averaged oEPSCs amplitude
658 before (baseline) and 25-30 min after LTD induction (LTD) in D2 MSNs with or without CPZ or SR
659 (D2 CPZ, p=0.0068; SR, p=0.9546 paired t-test). n represents the number of mice. All values are
660 represented as mean ± SEM, * $p<0.05$ paired t-test.
661

REFERENCES

Abela AR, Duan Y, Chudasama Y (2015) Hippocampal interplay with the nucleus accumbens is critical for decisions about time. European Journal of Neuroscience 42:2224–2233.

Ade K, Wan Y, Chen M, Gloss B, Calakos N (2011) An Improved BAC Transgenic Fluorescent Reporter Line for Sensitive and Specific Identification of Striatonigral Medium Spiny Neurons. Front Syst Neurosci 5 Available at: https://www.frontiersin.org/articles/10.3389/fnsys.2011.00032/full [Accessed February 2, 2019].

Ambroggi F, Ishikawa A, Fields HL, Nicola SM (2008) Basolateral Amygdala Neurons Facilitate Reward-Seeking Behavior by Exciting Nucleus Accumbens Neurons. Neuron 59:648–661.

Andersen SL, Rutstein M, Benzo JM, Hostetter JC, Teicher MH (1997) Sex differences in dopamine receptor overproduction and elimination. Neuroreport 8:1495–1498.

Andersen SL, Teicher MH (2000) Sex differences in dopamine receptors and their relevance to ADHD. Neurosci Biobehav Rev 24:137–141.

Araque A, Castillo PE, Manzoni OJ, Tonini R (2017) Synaptic functions of endocannabinoid signaling in health and disease. Neuropharmacology 124:13–24.

Bara A, Manduca A, Bernabeu A, Borsoi M, Serviado M, Lassalle O, Murphy M, Wager-Miller J, Mackie K, Pelissier-Alicot A-L, Trezza V, Manzoni OJ (2018) Sex-dependent effects of in utero cannabinoid exposure on cortical function. Elife 7.

Belleau ML, Warren RA (2000) Postnatal Development of Electrophysiological Properties of Nucleus Accumbens Neurons. Journal of Neurophysiology 84:2204–2216.

Bertran-Gonzalez J, Bosch C, Maroteaux M, Matamales M, Hervé D, Valjent E, Girault J-A (2008) Opposing Patterns of Signaling Activation in Dopamine D1 and D2 Receptor-Expressing Striatal Neurons in Response to Cocaine and Haloperidol. J Neurosci 28:5671–5685.

Beyeler A, Chang C-J, Silvestre M, Lévêque C, Namburi P, Wildes CP, Tye KM (2018) Organization of Valence-Encoding and Projection-Defined Neurons in the Basolateral Amygdala. Cell Reports 22:905–918.

Beyeler A, Namburi P, Glober GF, Simonnet C, Calhoon GG, Conyers GF, Luck R, Wildes CP, Tye KM (2016) Divergent Routing of Positive and Negative Information from the Amygdala during Memory Retrieval. Neuron 90:348–361.

Bosch-Bouju C, Larrieu T, Linders L, Manzoni OJ, Layé S (2016) Endocannabinoid-Mediated Plasticity in Nucleus Accumbens Controls Vulnerability to Anxiety after Social Defeat Stress. Cell Rep 16:1237–1242.

Britt JP, Benaliouad F, McDevitt RA, Stuber GD, Wise RA, Bonci A (2012) Synaptic and behavioral profile of multiple glutamatergic inputs to the nucleus accumbens. Neuron 76:790–803.

Butler AK, Uryu K, Rougon G, Chesselet MF (1999) N-methyl-D-aspartate receptor blockade affects polysialylated neural cell adhesion molecule expression and synaptic density during striatal development. Neuroscience 89:1169–1181.

Cao J, Dorris DM, Meitzen J (2018) Electrophysiological properties of medium spiny neurons in the nucleus accumbens core of prepubertal male and female Drd1a-tdTomato line 6 BAC transgenic mice. Journal of Neurophysiology Available at: https://www.physiology.org/doi/abs/10.1152/jn.00257.2018 [Accessed July 11, 2018].

Cardinal RN, Howes NJ (2005) Effects of lesions of the nucleus accumbens core on choice between small certain rewards and large uncertain rewards in rats. BMC Neuroscience 6:37.

Christakou A, Robbins TW, Everitt BJ (2001) Functional disconnection of a prefrontal cortical–dorsal striatal system disrupts choice reaction time performance: Implications for attentional function. Behavioral Neuroscience 115:812–825.

Christakou A, Robbins TW, Everitt BJ (2004) Prefrontal Cortical–Ventral Striatal Interactions Involved in Affective Modulation of Attentional Performance: Implications for Corticostriatal Circuit Function. J Neurosci 24:773–780.

Cools R, Sheridan M, Jacobs E, D'Esposito M (2007) Impulsive Personality Predicts Dopamine-Dependent Changes in Frontostriatal Activity during Component Processes of Working Memory. J Neurosci 27:5506–5514.

Eichenbaum H (2014) Time cells in the hippocampus: a new dimension for mapping memories. Nat Rev Neurosci 15:732–744.

Enoksson T, Bertran-Gonzalez J, Christie MJ (2012) Nucleus accumbens D2- and D1-receptor expressing medium spiny neurons are selectively activated by morphine withdrawal and acute morphine, respectively. Neuropharmacology 62:2463–2471.

Everitt BJ, Cardinal RN, Parkinson JA, Robbins TW (2003) Appetitive Behavior. Annals of the New York Academy of Sciences 985:233–250.

Everitt BJ, Morris KA, O'Brien A, Robbins TW (1991) The basolateral amygdala-ventral striatal system and conditioned place preference: Further evidence of limbic-striatal interactions underlying reward-related processes. Neuroscience 42:1–18.

Fernando ABP, Murray JE, Milton AL (2013) The amygdala: securing pleasure and avoiding pain. Front Behav Neurosci 7 Available at: https://www.ncbi.nlm.nih.gov/pmc/articles/PMC3854486/ [Accessed July 12, 2018].

Finch DM (1996) Neurophysiology of converging synaptic inputs from the rat prefrontal cortex, amygdala, midline thalamus, and hippocampal formation onto single neurons of the caudate/putamen and nucleus accumbens. Hippocampus 6:495–512.

Floresco SB (2015) The Nucleus Accumbens: An Interface Between Cognition, Emotion, and Action. Annual Review of Psychology 66:25–52.

734 Floresco SB, Braaksma DN, Phillips AG (1999) Thalamic–Cortical–Striatal Circuitry Subserves
735 Working Memory during Delayed Responding on a Radial Arm Maze. J Neurosci
736 19:11061–11071.

737 Floresco SB, Seamans JK, Phillips AG (1997) Selective Roles for Hippocampal, Prefrontal Cortical,
738 and Ventral Striatal Circuits in Radial-Arm Maze Tasks With or Without a Delay. J
739 Neurosci 17:1880–1890.

740 Francis TC, Chandra R, Friend DM, Finkel E, Dayrit G, Miranda J, Brooks JM, Iñiguez SD,
741 O'Donnell P, Kravitz A, Lobo MK (2015) Nucleus Accumbens Medium Spiny Neuron
742 Subtypes Mediate Depression-Related Outcomes to Social Defeat Stress. Biological
743 Psychiatry 77:212–222.

744 French SJ, Totterdell S (2002) Hippocampal and prefrontal cortical inputs monosynaptically
745 converge with individual projection neurons of the nucleus accumbens. J Comp Neurol
746 446:151–165.

747 French SJ, Totterdell S (2003) Individual nucleus accumbens-projection neurons receive both
748 basolateral amygdala and ventral subicular afferents in rats. Neuroscience 119:19–31.

749 Gerdeman GL, Ronesi J, Lovinger DM (2002) Postsynaptic endocannabinoid release is critical to
750 long-term depression in the striatum. Nature Neuroscience 5:446–451.

751 Gertler TS, Chan CS, Surmeier DJ (2008) Dichotomous Anatomical Properties of Adult Striatal
752 Medium Spiny Neurons. J Neurosci 28:10814–10824.

753 Gibson HE, Edwards JG, Page RS, Van Hook MJ, Kauer JA (2008) TRPV1 channels mediate long-
754 term depression at synapses on hippocampal interneurons. Neuron 57:746–759.

755 Goda Y, Stevens CF (1994) Two components of transmitter release at a central synapse. Proc
756 Natl Acad Sci USA 91:12942–12946.

757 Goto Y, Grace AA (2008) Limbic and cortical information processing in the nucleus accumbens.
758 Trends in Neurosciences 31:552–558.

759 Goto Y, O'Donnell P (2001) Network Synchrony in the Nucleus Accumbens In Vivo. J Neurosci
760 21:4498–4504.

761 Groenewegen HJ, Wright CI, Beijer AV j., Voorn P (1999) Convergence and Segregation of
762 Ventral Striatal Inputs and Outputs. Annals of the New York Academy of Sciences
763 877:49–63.

764 Grueter BA, Brasnjo G, Malenka RC (2010) Postsynaptic TRPV1 triggers cell type–specific long-
765 term depression in the nucleus accumbens. Nature Neuroscience 13:1519–1525.

766 Hernández-López S, Bargas J, Surmeier DJ, Reyes A, Galarraga E (1997) D1 Receptor Activation
767 Enhances Evoked Discharge in Neostriatal Medium Spiny Neurons by Modulating an L-
768 Type Ca2+ Conductance. J Neurosci 17:3334–3342.

769 Hernández-López S, Tkatch T, Perez-Garci E, Galarraga E, Bargas J, Hamm H, Surmeier DJ (2000)
770 D2 Dopamine Receptors in Striatal Medium Spiny Neurons Reduce L-Type Ca2+ Currents
771 and Excitability via a Novel PLCβ1–IP3–Calcineurin-Signaling Cascade. J Neurosci
772 20:8987–8995.

773 Humphries MD, Prescott TJ (2010) The ventral basal ganglia, a selection mechanism at the
774 crossroads of space, strategy, and reward. Progress in Neurobiology 90:385–417.

775 Ito R, Robbins TW, Pennartz CM, Everitt BJ (2008) Functional Interaction between the
776 Hippocampus and Nucleus Accumbens Shell Is Necessary for the Acquisition of
777 Appetitive Spatial Context Conditioning. J Neurosci 28:6950–6959.

778 Jung K-M, Sepers M, Henstridge CM, Lassalle O, Neuhofer D, Martin H, Ginger M, Frick A,
779 DiPatrizio NV, Mackie K, Katona I, Piomelli D, Manzoni OJ (2012) Uncoupling of the
780 endocannabinoid signalling complex in a mouse model of fragile X syndrome. Nat
781 Commun 3:1080.

782 Kasanetz F, Deroche-Gamonet V, Berson N, Balado E, Lafourcade M, Manzoni O, Piazza PV
783 (2010) Transition to addiction is associated with a persistent impairment in synaptic
784 plasticity. Science 328:1709–1712.

785 Kasanetz F, Manzoni OJ (2009) Maturation of excitatory synaptic transmission of the rat nucleus
786 accumbens from juvenile to adult. J Neurophysiol 101:2516–2527.

787 Kreitzer AC, Malenka RC (2007) Endocannabinoid-mediated rescue of striatal LTD and motor
788 deficits in Parkinson's disease models. Nature 445:643–647.

789 Lafourcade M, Elezgarai I, Mato S, Bakiri Y, Grandes P, Manzoni OJ (2007) Molecular
790 Components and Functions of the Endocannabinoid System in Mouse Prefrontal Cortex.
791 PLOS ONE 2:e709.

792 Lafourcade M, Larrieu T, Mato S, Duffaud A, Sepers M, Matias I, De Smedt-Peyrusse V,
793 Labrousse VF, Bretillon L, Matute C, Rodríguez-Puertas R, Layé S, Manzoni OJ (2011)
794 Nutritional omega-3 deficiency abolishes endocannabinoid-mediated neuronal
795 functions. Nat Neurosci 14:345–350.

796 LeDoux J (2003) The emotional brain, fear, and the amygdala. Cell Mol Neurobiol 23:727–738.

797 Li Z, Chen Z, Fan G, Li A, Yuan J, Xu T (2018) Cell-Type-Specific Afferent Innervation of the
798 Nucleus Accumbens Core and Shell. Front Neuroanat 12 Available at:
799 https://www.ncbi.nlm.nih.gov/pmc/articles/PMC6232828/ [Accessed January 2, 2019].

800 Lobo MK, Nestler EJ (2011) The Striatal Balancing Act in Drug Addiction: Distinct Roles of Direct
801 and Indirect Pathway Medium Spiny Neurons. Front Neuroanat 5 Available at:
802 https://www.frontiersin.org/articles/10.3389/fnana.2011.00041/full [Accessed January
803 15, 2019].

804 Ma Y-Y, Cepeda C, Chatta P, Franklin L, Evans CJ, Levine MS (2012) Regional and cell-type-
805 specific effects of DAMGO on striatal D1 and D2 dopamine receptor-expressing
806 medium-sized spiny neurons. ASN Neuro 4.

807 Ma Y-Y, Lee BR, Wang X, Guo C, Liu L, Cui R, Lan Y, Balcita-Pedicino JJ, Wolf ME, Sesack SR,
808 Shaham Y, Schlüter OM, Huang YH, Dong Y (2014) Bidirectional Modulation of
809 Incubation of Cocaine Craving by Silent Synapse-Based Remodeling of Prefrontal Cortex
810 to Accumbens Projections. Neuron 83:1453–1467.

811 Manduca A, Bara A, Larrieu T, Lassalle O, Joffre C, Layé S, Manzoni OJ (2017) Amplification of
812 mGlu5-Endocannabinoid Signaling Rescues Behavioral and Synaptic Deficits in a Mouse
813 Model of Adolescent and Adult Dietary Polyunsaturated Fatty Acid Imbalance. J
814 Neurosci 37:6851–6868.

815 Mannella F, Gurney K, Baldassarre G (2013) The nucleus accumbens as a nexus between values
816 and goals in goal-directed behavior: a review and a new hypothesis. Front Behav
817 Neurosci 7 Available at:
818 https://www.frontiersin.org/articles/10.3389/fnbeh.2013.00135/full [Accessed
819 December 25, 2017].

820 Martin HGS, Lassalle O, Manzoni OJ (2017) Differential Adulthood Onset mGlu5 Signaling Saves
821 Prefrontal Function in the Fragile X Mouse. Cereb Cortex 27:5592–5602.

822 McGarry LM, Carter AG (2017) Prefrontal cortex drives distinct projection neurons in the
823 basolateral amygdala. Cell Rep 21:1426–1433.

824 McGinty VB, Grace AA (2009) Timing-Dependent Regulation of Evoked Spiking in Nucleus
825 Accumbens Neurons by Integration of Limbic and Prefrontal Cortical Inputs. J
826 Neurophysiol 101:1823–1835.

827 McLaughlin RJ, Floresco SB (2007) The role of different subregions of the basolateral amygdala
828 in cue-induced reinstatement and extinction of food-seeking behavior. Neuroscience
829 146:1484–1494.

830 Micale V, Cristino L, Tamburella A, Petrosino S, Leggio GM, Drago F, Di Marzo V (2009)
831 Anxiolytic effects in mice of a dual blocker of fatty acid amide hydrolase and transient
832 receptor potential vanilloid type-1 channels. Neuropsychopharmacology 34:593–606.

833 Musella A, De Chiara V, Rossi S, Prosperetti C, Bernardi G, Maccarrone M, Centonze D (2009)
834 TRPV1 channels facilitate glutamate transmission in the striatum. Molecular and Cellular
835 Neuroscience 40:89–97.

836 Neuhofer D, Henstridge CM, Dudok B, Sepers M, Lassalle O, Katona I, Manzoni OJ (2015)
837 Functional and structural deficits at accumbens synapses in a mouse model of Fragile X.
838 Frontiers in Cellular Neuroscience 9 Available at:
839 http://www.frontiersin.org/Cellular_Neuroscience/10.3389/fncel.2015.00100/abstract
840 [Accessed February 7, 2019].

841 Neuhofer D, Lassalle O, Manzoni OJ (2018) Muscarinic M1 Receptor Modulation of Synaptic
842 Plasticity in Nucleus Accumbens of Wild-Type and Fragile X Mice. ACS Chem Neurosci
843 9:2233–2240.

844 Nisenbaum ES, Xu ZC, Wilson CJ (1994) Contribution of a slowly inactivating potassium current
845 to the transition to firing of neostriatal spiny projection neurons. J Neurophysiol
846 71:1174–1189.

847 O'Donnell P, Grace AA (1995) Synaptic interactions among excitatory afferents to nucleus
848 accumbens neurons: hippocampal gating of prefrontal cortical input. J Neurosci
849 15:3622–3639.

850 Planert H, Berger TK, Silberberg G (2013) Membrane Properties of Striatal Direct and Indirect
851 Pathway Neurons in Mouse and Rat Slices and Their Modulation by Dopamine. PLOS
852 ONE 8:e57054.

853 Qi J, Zhang S, Wang H-L, Barker DJ, Miranda-Barrientos J, Morales M (2016) VTA glutamatergic
854 inputs to nucleus accumbens drive aversion by acting on GABAergic interneurons.
855 Nature Neuroscience 19:725–733.

856 Robbe D, Alonso G, Duchamp F, Bockaert J, Manzoni OJ (2001) Localization and Mechanisms of
857 Action of Cannabinoid Receptors at the Glutamatergic Synapses of the Mouse Nucleus
858 Accumbens. J Neurosci 21:109–116.

859 Robbe D, Kopf M, Remaury A, Bockaert J, Manzoni OJ (2002) Endogenous cannabinoids mediate
860 long-term synaptic depression in the nucleus accumbens. PNAS 99:8384–8388.

861 Rogers-Carter MM, Djerdjaj A, Gribbons KB, Varela J, Christianson JP (2019) Insular cortex
862 projections to nucleus accumbens core mediate social approach to stressed juvenile
863 rats. bioRxiv Available at: http://biorxiv.org/lookup/doi/10.1101/544221 [Accessed
864 February 28, 2019].

865 Salgado S, Kaplitt MG (2015) The Nucleus Accumbens: A Comprehensive Review. Stereotactic
866 and Functional Neurosurgery 93:75–93.

867 Sesack SR, Grace AA (2010) Cortico-Basal Ganglia Reward Network: Microcircuitry.
868 Neuropsychopharmacology 35:27–47.

869 Shen C-J, Zheng D, Li K-X, Yang J-M, Pan H-Q, Yu X-D, Fu J-Y, Zhu Y, Sun Q-X, Tang M-Y, Zhang Y,
870 Sun P, Xie Y, Duan S, Hu H, Li X-M (2019) Cannabinoid CB 1 receptors in the amygdalar
871 cholecystokinin glutamatergic afferents to nucleus accumbens modulate depressive-like
872 behavior. Nature Medicine:1.

873 Shiflett MW, Balleine BW (2010) At the limbic–motor interface: disconnection of basolateral
874 amygdala from nucleus accumbens core and shell reveals dissociable components of
875 incentive motivation. European Journal of Neuroscience 32:1735–1743.

876 Silver RA, Momiyama A, Cull-Candy SG (1998) Locus of frequency-dependent depression
877 identified with multiple-probability fluctuation analysis at rat climbing fibre-Purkinje cell
878 synapses. J Physiol (Lond) 510 (Pt 3):881–902.

879 Stratford TR, Wirtshafter D (2013) Injections of muscimol into the paraventricular thalamic
880 nucleus, but not mediodorsal thalamic nuclei, induce feeding in rats. Brain Res
881 1490:128–133.

882 Tepper JM, Sharpe NA, Koós TZ, Trent F (1998) Postnatal development of the rat neostriatum:
883 electrophysiological, light- and electron-microscopic studies. Dev Neurosci 20:125–145.

884 Thibault D, Loustalot F, Fortin GM, Bourque M-J, Trudeau L-É (2013) Evaluation of D1 and D2
885 Dopamine Receptor Segregation in the Developing Striatum Using BAC Transgenic Mice.
886 PLOS ONE 8:e67219.

887 Thomazeau A, Bosch-Bouju C, Manzoni O, Layé S (2017) Nutritional n-3 PUFA Deficiency
888 Abolishes Endocannabinoid Gating of Hippocampal Long-Term Potentiation. Cereb
889 Cortex 27:2571–2579.

890 Thomazeau A, Lassalle O, Iafrati J, Souchet B, Guedj F, Janel N, Chavis P, Delabar J, Manzoni OJ
891 (2014) Prefrontal deficits in a murine model overexpressing the down syndrome
892 candidate gene dyrk1a. J Neurosci 34:1138–1147.

893 Trouche S, Koren V, Doig NM, Ellender TJ, Lopes-dos-Santos V, Perestenko PV, El-Gaby M, Garas
894 FN, Magill PJ, Sharott A, Dupret D (2018) A Dorsal Hippocampus-Accumbens Circuit
895 Motif to Guide Appetitive Memory in Space. Rochester, NY: Social Science Research
896 Network. Available at: https://papers.ssrn.com/abstract=3188482 [Accessed January 27,
897 2019].

898 Tye KM, Prakash R, Kim S-Y, Fenno LE, Grosenick L, Zarabi H, Thompson KR, Gradinaru V,
899 Ramakrishnan C, Deisseroth K (2011) Amygdala circuitry mediating reversible and
900 bidirectional control of anxiety. Nature 471:358–362.

901 Wu Y-W, Kim J-I, Tawfik VL, Lalchandani RR, Scherrer G, Ding JB (2015) Input- and Cell Type-
902 Specific Endocannabinoid-Dependent LTD in the Striatum. Cell Rep 10:75–87.

903 Yizhar O, Fenno LE, Davidson TJ, Mogri M, Deisseroth K (2011) Optogenetics in neural systems.
904 Neuron 71:9–34.

905 Zahm DS, Brog JS (1992) On the significance of subterritories in the “accumbens” part of the rat
906 ventral striatum. Neuroscience 50:751–767.

907 Zhang L, Warren RA (2008) Postnatal development of excitatory postsynaptic currents in
908 nucleus accumbens medium spiny neurons. Neuroscience 154:1440–1449.

909 Zhu Y, Wienecke CFR, Nachtrab G, Chen X (2016) A thalamic input to the nucleus accumbens
910 mediates opiate dependence. Nature 530:219–222.

911

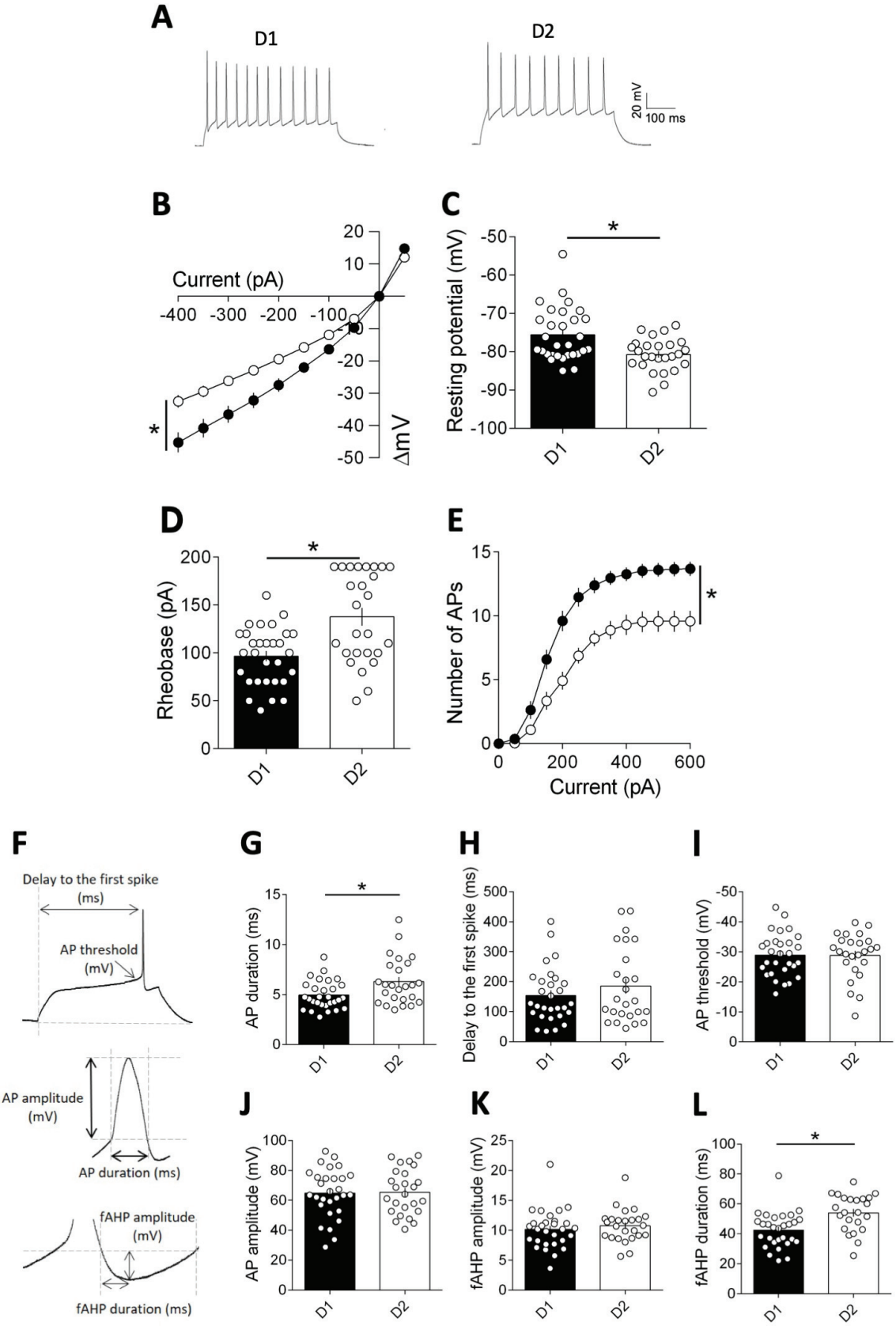

Figure 1

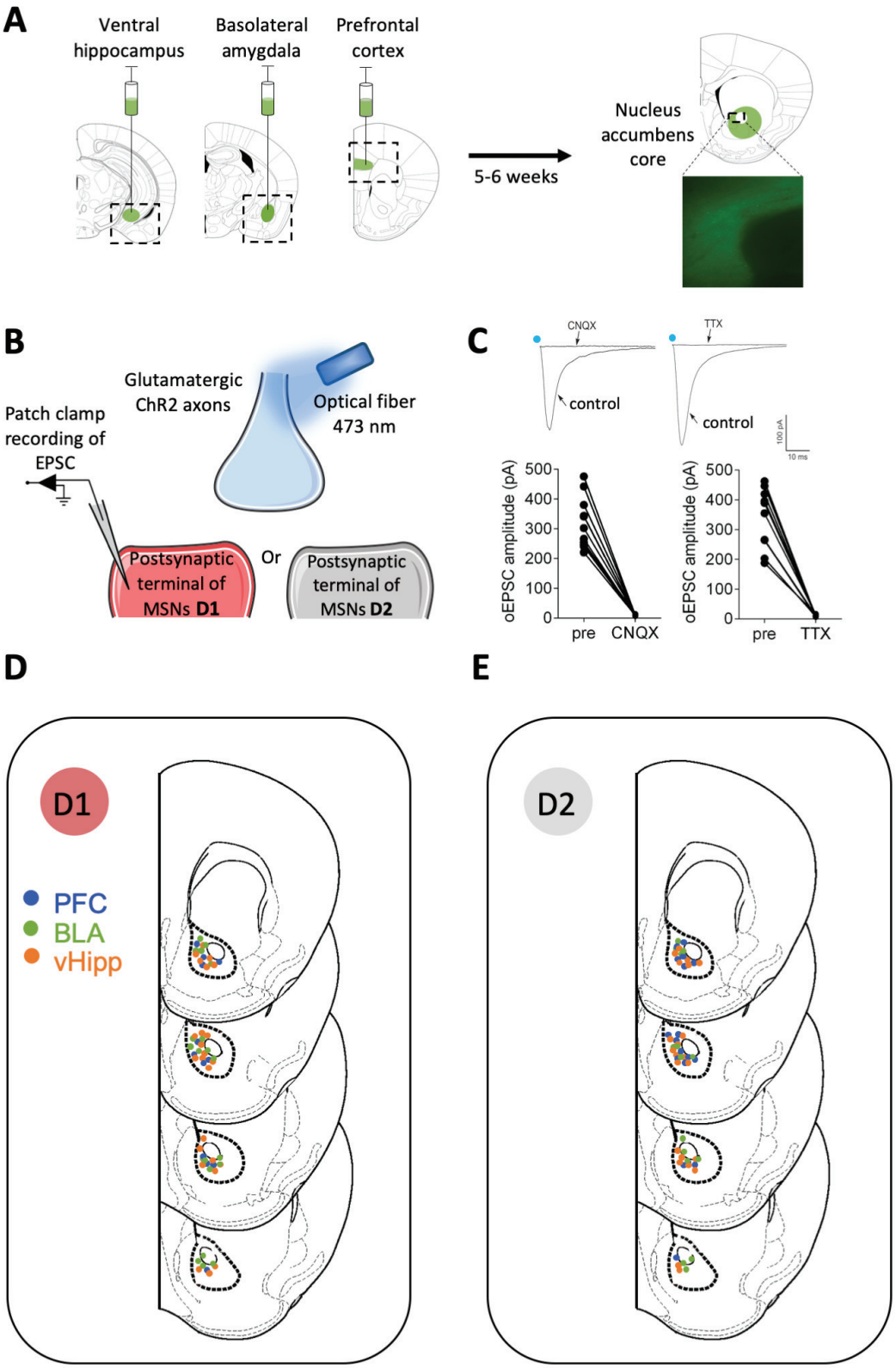

Figure 2

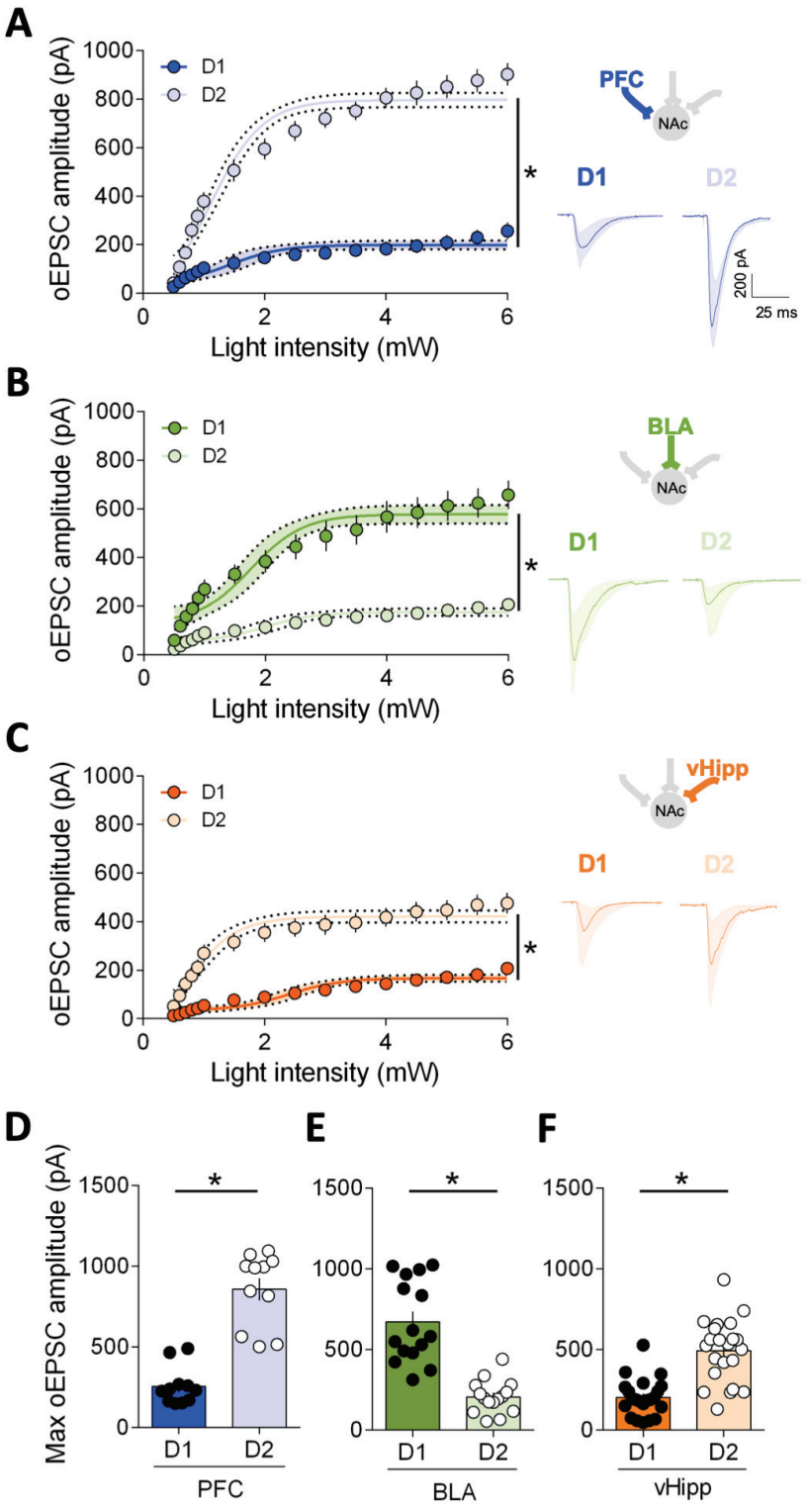

Figure 3

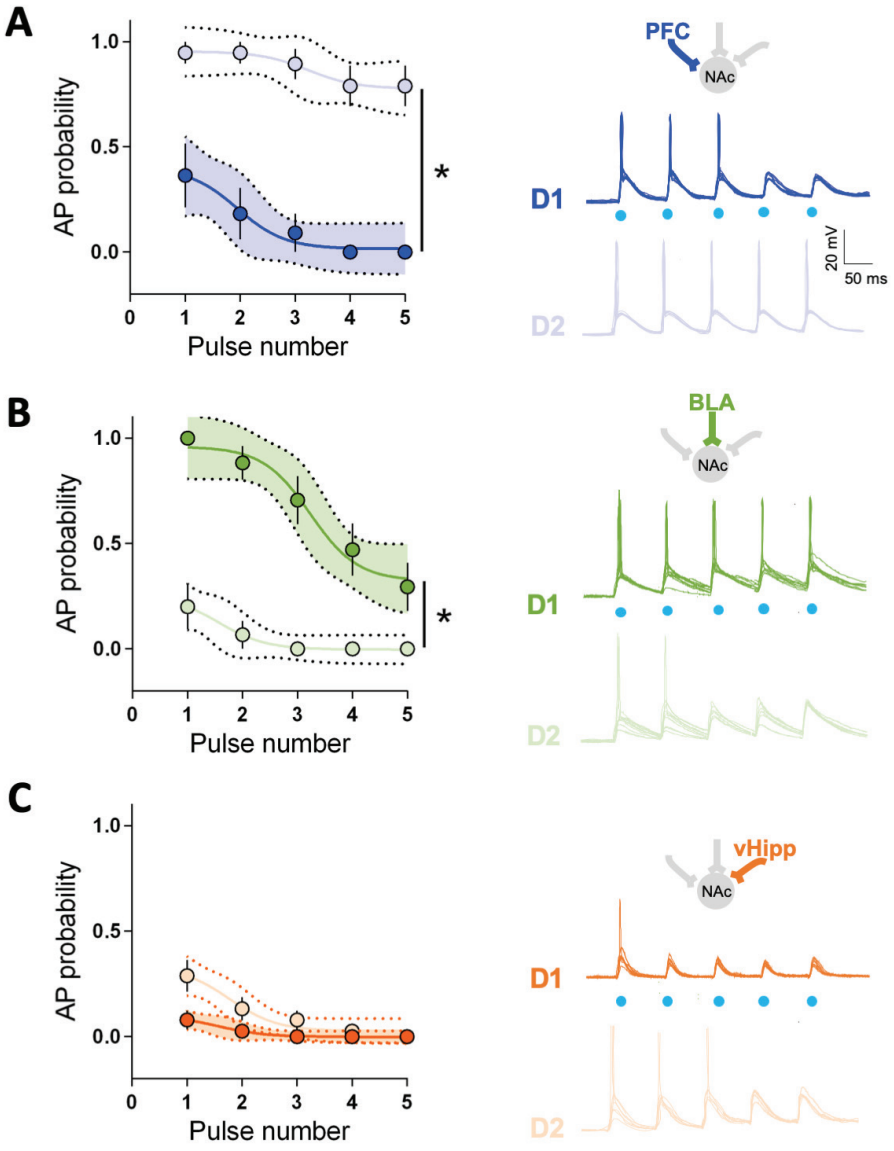

Figure 4

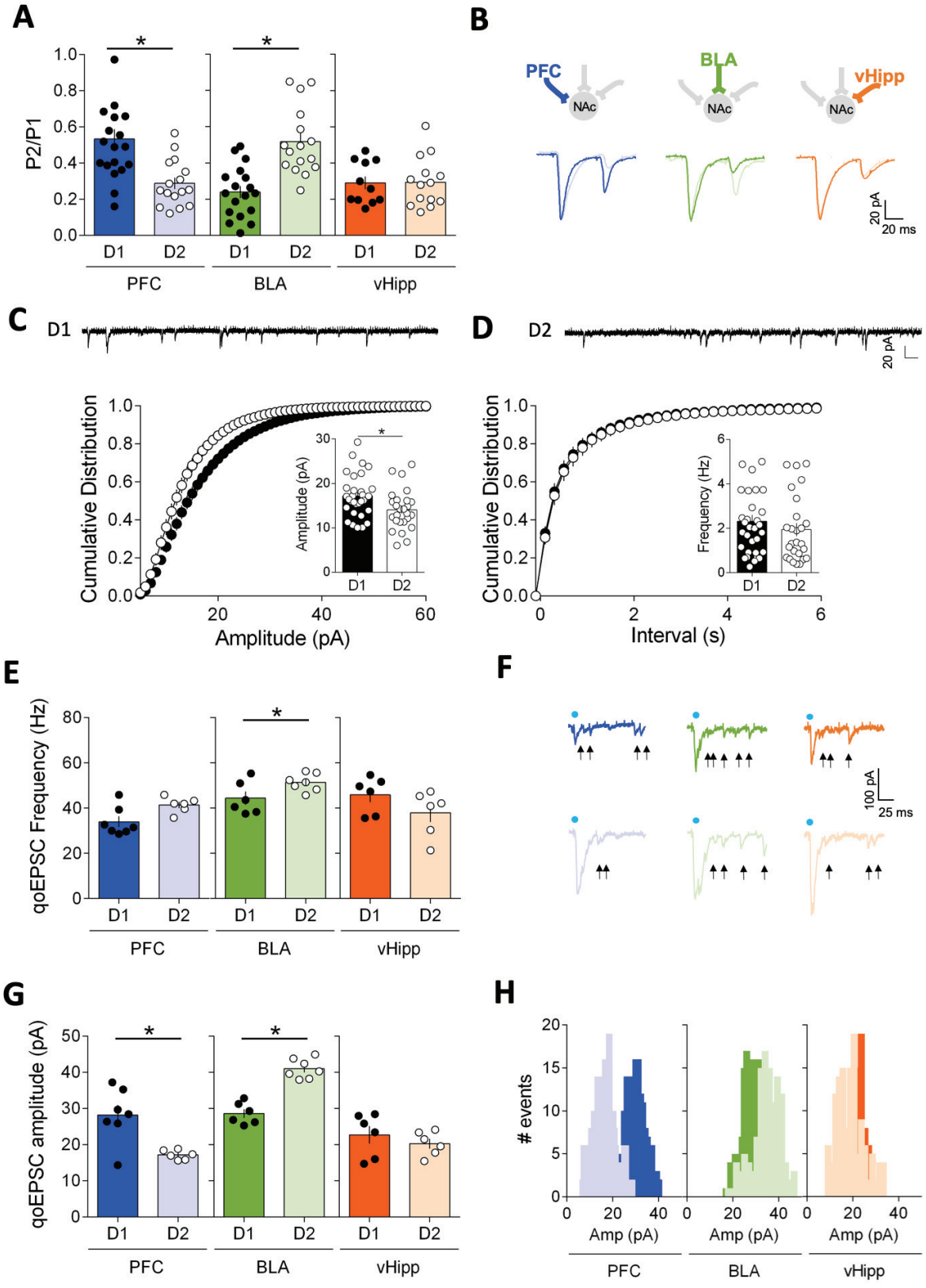

Figure 5

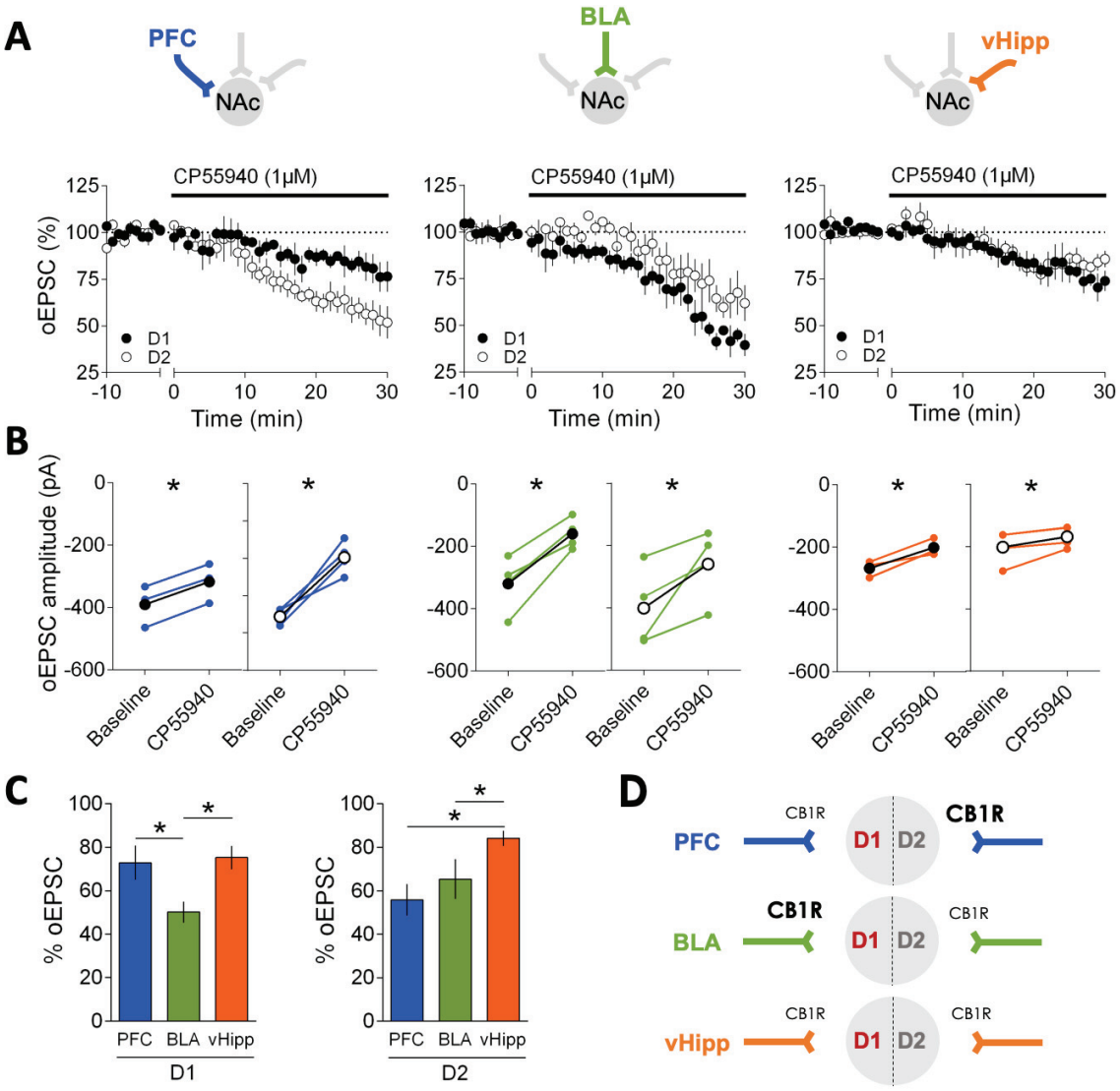

Figure 6

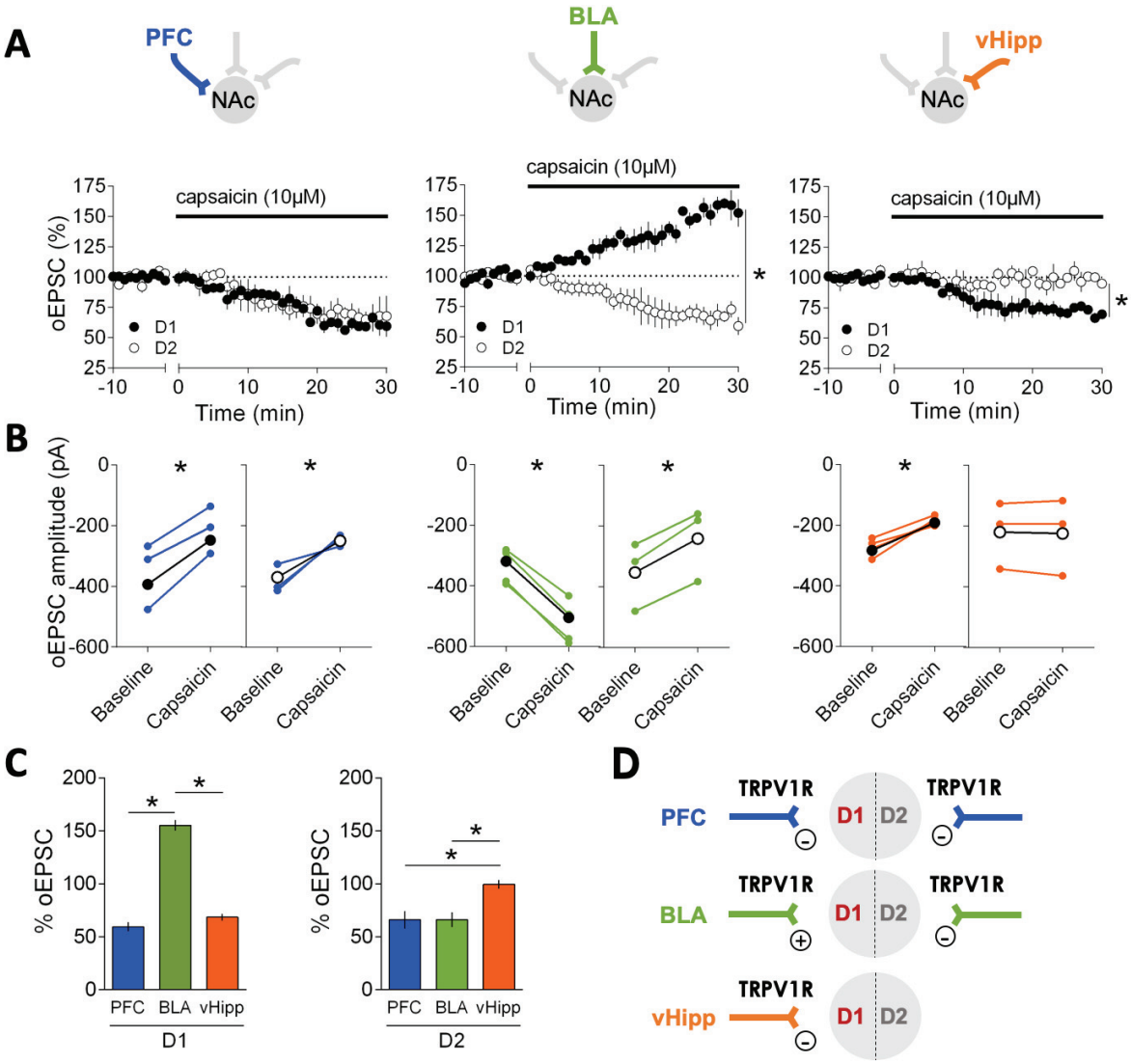

Figure 7

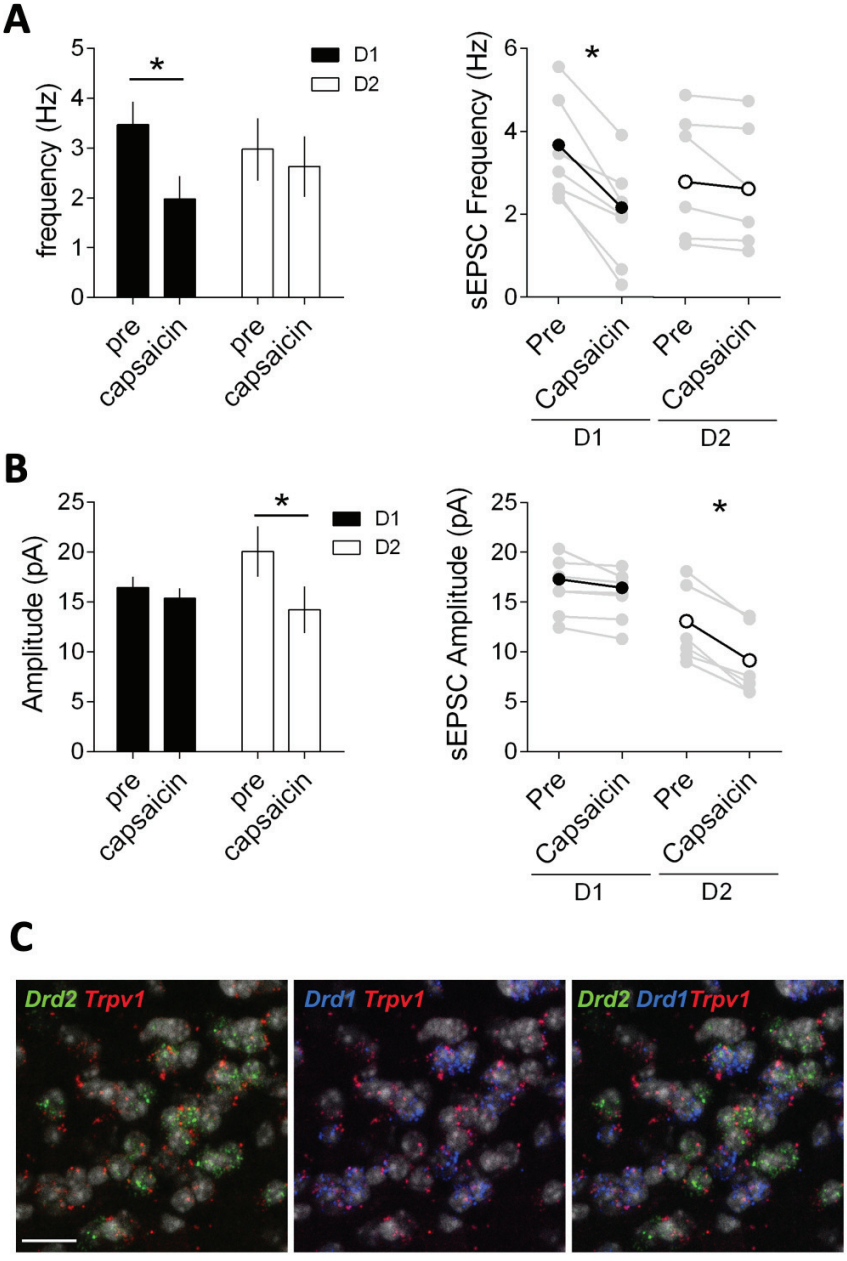

Figure 8

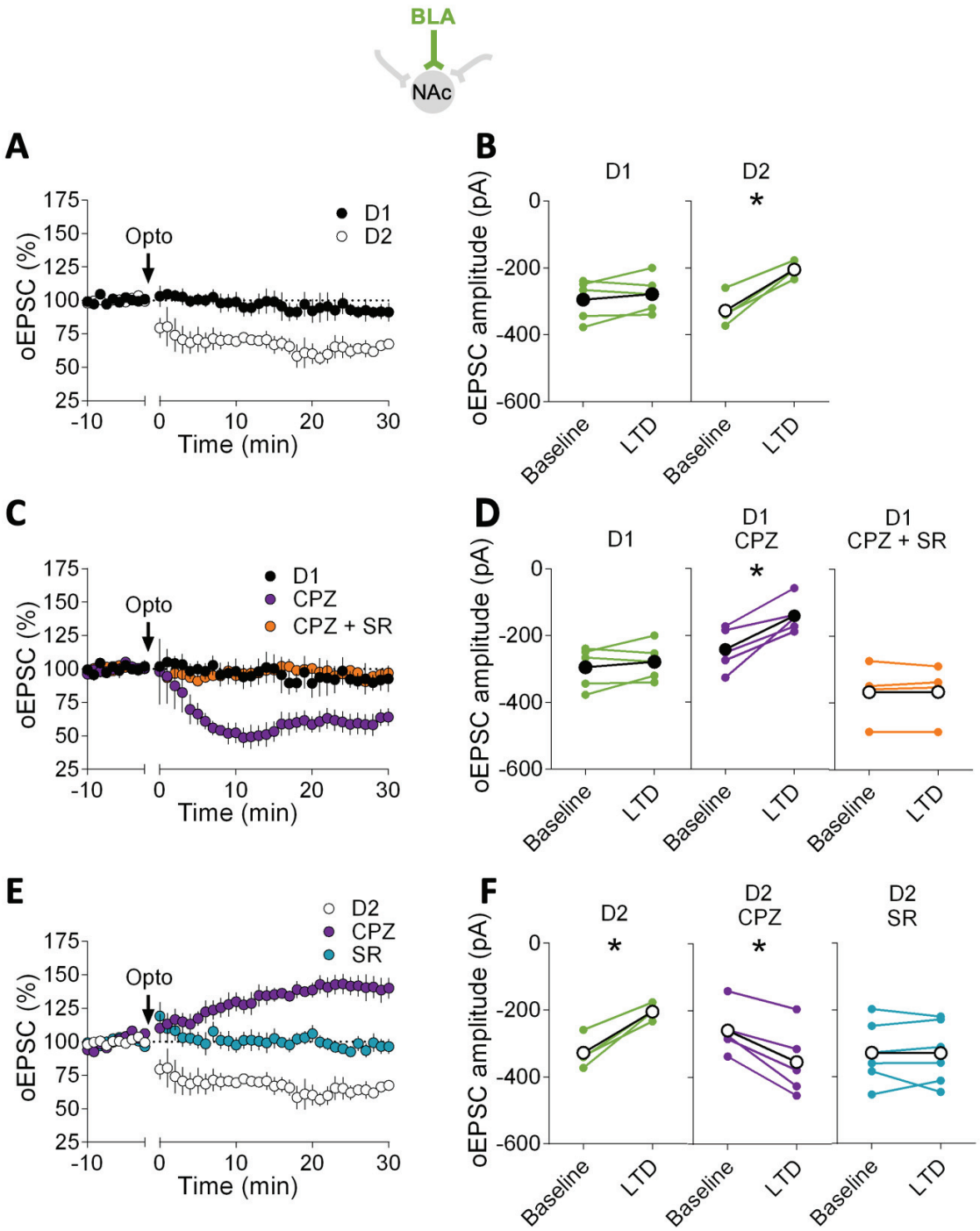

Figure 9